

Modelling Airborne L-band Radar Sea and Coastal Land Clutter

Poh Lian Choong

DSTO-TR-0945

DISTRIBUTION STATEMENT A
Approved for Public Release
Distribution Unlimited

DQC QUALITY INSPECTED 4
20000822 123

Modelling Airborne L-band Radar Sea and Coastal Land Clutter

Poh Lian Choong

Surveillance Systems Division
Electronics and Surveillance Research Laboratory

DSTO-TR-0945

ABSTRACT

The limiting factor affecting the performance of most airborne radar systems in detecting targets on or near wind-swept surface of the sea is return echoes from sea surface known as sea clutter. This report addresses the clutter returns from a maritime environment for airborne L-band VV-polarised radar. Modelling of radar sea return is discussed with consideration to propagation under standard atmospheric conditions. A composite sea clutter model has been developed, which is based upon the concept of a two-scale sea surface model with directional sea spectrum and simple facet specular return at near-normal incidence. Several sea clutter models have been collated with data collected by the Naval Research Laboratory four-frequency radar system under varying sea conditions, and polarimetric synthetic aperture radar images of the North-West of Australia. The results of the comparison have shown that the composite sea clutter model better predicts the backscattering coefficient, σ^0 , of sea surface returns for varying sea conditions, radar look directions, and grazing angles. In addition, a radar backscattering model for bare soil showed good agreement between modelling results and POLSAR data for returns from coastal saline flat surfaces surrounding the North-West coastal areas.

APPROVED FOR PUBLIC RELEASE

DEPARTMENT OF DEFENCE
DEFENCE SCIENCE & TECHNOLOGY ORGANISATION

DSTO

AQF00-11-3096

DSTO-TR-0945

Published by

DSTO Electronics and Surveillance Research Laboratory

PO Box 1500

Salisbury, South Australia, Australia 5108

Telephone: (08) 8259 5555

Facsimile: (08) 8259 6567

© Commonwealth of Australia 2000

AR No. AR-011-227

March 2000

APPROVED FOR PUBLIC RELEASE

Modelling Airborne L-band Radar Sea and Coastal Land Clutter

EXECUTIVE SUMMARY

This report represents the result of a study performed under the task AIR99/047-“AEW&C SUPPORT”. The performance of an L-band Airborne Early Warning and Control (AEW&C) radar system in detecting targets in a maritime environment is significantly affected by clutter backscatter from the sea surface and coastal land areas. A thorough understanding of these return signals is vital in assessing the performance of the radar in detecting targets over sea and site-specific coastal land areas. An essential ingredient in this development is the need to accurately model sea surface and site-specific coastal land areas reflection or backscatter signals.

The primary objective of this study is to develop an L-band VV-polarised sea clutter model to quantitatively predict the radar sea backscattering coefficient, σ° , as a function of radar parameters, and sea surface conditions under standard atmospheric conditions. This report looks at several semi-empirical sea clutter models and their relation to modelling backscattering from the sea surface for varying sea conditions, grazing angles and radar look directions for an L-band radar. In addition, a second-order composite sea clutter model has been developed, which is based upon the concept of the two-scale sea surface model to predict the L-band radar sea backscattering coefficient, σ° , for varying sea conditions, grazing angles and radar look directions.

These semi-empirical sea clutter models and the second-order composite sea clutter model have been collated with data collected by the Naval Research Laboratory four-frequency radar system under varying sea conditions and polarimetric synthetic aperture radar images of the North-West of Australia. The results of the comparison have shown that the second-order composite sea clutter model better predicts the backscattering coefficient, σ° , of sea surface returns for a wide range of grazing angles, radar look directions and sea conditions. The composite sea clutter model also showed good agreement between the modelling result and POLSAR data for shallow water returns from the coastal water surface surrounding the Darwin area for grazing angles between 25° to 65°.

The secondary objective of this study is to develop an L-band VV-polarised land clutter model to quantitatively predict the radar backscattering coefficient, σ° , from coastal land areas. The radar backscattering model developed for predicting microwave scattering from bare soil surface showed good agreement between its modelling results and measured backscatter values from coastal saline flats surrounding the North-West coastal areas.

DSTO-TR-0945

Authors

Poh Lian Choong

Surveillance Systems Division

Dr. Poh Lian Choong received her B.E. (Hons) degree in electrical and electronic engineering from the University of Auckland, New Zealand and Ph.D. degree from the University of Western Australia, Australia. From 1998, she has worked in Surveillance Systems Division as a Research Scientist. Her research interests include: (1) modelling and simulation of land and sea clutter for radar performance analysis; and (2) development of Artificial Neural Networks, Syntactic Pattern Recognition, Maximum Entropy and Bayesian methodologies in application to automatic pattern recognition and classification.

DSTO-TR-0945

Contents

Glossary	xi
1 Introduction	1
2 Backscattering from the Sea Surface in Standard Atmospheric Conditions (σ°)	2
2.1 Dependence on Radar Grazing Angle	2
2.1.1 Quasi-Specular Grazing Angle Region	3
2.1.2 Plateau or Bragg Backscattering Region	3
2.1.3 Low Grazing Angle Region	4
2.2 Dependence on Wind Speed	5
2.3 Dependence on Wind Direction	6
2.4 Dependence on Rain	6
3 Data Source for L Band	7
3.1 Naval Research Laboratory Airborne Trials [46, 16, 8, 9]	7
3.2 Normalised Mean Backscattering Coefficient (σ°) compiled by Nathanson [29]	8
3.3 POLSAR Darwin Data	9
3.3.1 Study Area	9
3.3.2 SAR Terrain Analysis Program	14
4 Semi-Empirical Sea Clutter Models	16
4.1 The Use of Nathanson and NRL-4FR Data Sets to Test the GIT, HYB, and TSC Models	17
5 Composite Sea Clutter Models	20
5.1 Specular Backscattering for Fully Developed Sea	20
5.2 Two-Scale Bragg Model	22
5.2.1 First-Order Composite Sea Clutter Model (CSM), $\sigma_{B1(pp)}^\circ$	23
5.2.2 Second-Order Composite Sea Clutter Model (MCSM)	25
5.2.3 The Use of the NRL-4FR Data to Test the CSM and MCSM Models	26
6 Comparisons with Radar Measurements	28

7	Radar Backscattering Signals from Darwin Coastal Areas	36
7.1	Coastal Water Backscattering Characteristics	36
7.2	Wetland Features	37
7.2.1	Radar Backscattering from Coastal Saline Flat Surfaces (A) . . .	37
7.2.2	Radar Backscattering from Coastal Mangrove Forest	39
8	Conclusions	40

Appendices

A	POLSAR Mean Backscattering Coefficients, σ° (Darwin Data)	41
B	Semi-Empirical Sea Clutter Models	46
B.1	Georgia Institute of Technology (GIT) Sea Clutter Model	46
B.2	Hybrid (HYB) Sea Clutter Model [35, 1]	47
B.3	Technology Service Corporation (TSC) Sea Clutter Model [40]	48
	References	50

Figures

2.1	Relationship between grazing angle, polarisation and radar sea backscatter returns	2
2.2	Two-scale Sea Surface	4
2.3	Dependence of σ_m° on Wind Speed, Wave Height and Polarisation [26]	6
3.1	Location of the Study Area	9
3.2	Zonation of Mangroves - Darwin Harbour [3]	10
3.3	(a) <i>Ceriops tagal</i> low closed-forest (mid tidal flat), and (b) <i>Rhizophora stylosa</i> closed-forest/low closed-forest (shoreline forest) [3]	10
3.4	POLSAR Darwin L-band VV data (CM5512)	12
3.5	POLSAR Darwin L-band VV data (CM5148)	13
3.6	SAR Analysis GUI Interface	14
3.7	SAR Pixel Analysis GUI Interface	15
3.8	Normalised σ° coefficients from the sea surface (L-VV, $U = 3.88$ m/s)	15
4.1	Comparisons of Semi-Empirical Sea Clutter Models at L-band (VV-Pol. and Upwind): (a) Wind speed = 5.6 m/s, and (b) Wind speed = 12.1 m/s.	18

5.1	Grazing Angle Error due to Sea Surface Slope	21
5.2	CSM L-band Sea Clutter Model (1.228 GHz) [16]	24
5.3	Dependence of σ° on wind speed, U (L-band, VV-Pol. and upwind). (a) wind speed = 2.5 m/s; (b) wind speed = 5.6 m/s; (c) wind speed = 12.1 m/s; (d) wind speed = 16.3 m/s; (e) wind speed = 18.5 m/s; and (f) wind speed = 23.5 m/s	27
6.1	Dependence of σ_m° on Wind Speed, V_w (L-band, VV-Pol. and Upwind). (a) Wind speed = 5.6 m/s; (b) Wind speed = 12.1 m/s;	28
6.2	Dependence of σ° on wind speed - JOSH I, U (L-band, VV-Pol. and upwind). (a) wind speed = 5.8 m/s; (b) wind speed = 8.4 m/s; (c) wind speed = 11.55 m/s; (d) wind speed = 13.125 m/s	29
6.3	Dependence of σ° on wind speed - JOSH I, U (L-band, VV-Pol. and downwind). (a) wind speed = 5.8 m/s; (b) wind speed = 8.4 m/s; (c) wind speed = 11.55 m/s; (d) wind speed = 13.125 m/s	30
6.4	Dependence of σ° on wind speed - JOSH I, U (L-band, VV-Pol. and crosswind). (a) wind speed = 5.8 m/s; (b) wind speed = 8.4 m/s; (c) wind speed = 11.55 m/s; (d) wind speed = 13.125 m/s	31
6.5	Dependence of σ° on wind speed - JOSH II, U (L-band, VV-Pol. and upwind). (a) wind speed = 1.3125 m/s; (b) wind speed = 8.4 m/s; (c) wind speed = 13.6 m/s	32
6.6	Dependence of σ° on wind speed - JOSH II, U (L-band, VV-Pol. and downwind). (a) wind speed = 1.3125 m/s; (b) wind speed = 8.4 m/s; (c) wind speed = 13.6 m/s	33
6.7	Dependence of σ° on wind speed - JOSH II, U (L-band, VV-Pol. and crosswind). (a) wind speed = 1.3125 m/s; (b) wind speed = 8.4 m/s; (c) wind speed = 13.6 m/s	34
6.8	Dependence of σ° on Grazing Angle (L-VV, wind speed = 3.88 m/s)	35
7.1	Radar Backscattering Coefficients from Shallow Water Surface	36
7.2	Backscatter components of wetlands. A = surface backscatter. B = canopy backscatter. C = double bounce trunk-surface backscatter. D = double bounce aerial-surface backscatter. E = double bounce canopy-surface backscatter. [48]	37
7.3	Radar Backscattering from Coastal Saline Flat	38
7.4	L-VV Backscattering Prediction for Non-flooded Coastal Saline Flat Surfaces	39
7.5	Radar Backscattering from Mangrove Forest (L-VV)	40

Tables

3.1	POLSAR Specifications for the 23 November 1996 Darwin Deployment	11
-----	--	----

3.2	Hydro-meteor Parameters for the 23 November 1996 Darwin Deployment (Provided by Dr. Ed Kruzins, DSTO)	11
4.1	Semi-Empirical Sea Clutter Capabilities	17
A1	Backscattering Coefficient for Deep Water for L-VV POLSAR Darwin	42
A2	Backscattering Coefficient for Coastal Water for L-VV POLSAR Darwin . . .	43
A3	Backscattering Coefficient for Coastal Saline Flat for L-VV POLSAR Darwin	44
A4	Backscattering Coefficient for Mangrove Forest for L-VV POLSAR Darwin .	45

Glossary

ψ	Grazing angle (to horizontal axis, degrees)
θ_i	Incidence angle (to vertical axis, degrees)
θ_a	Azimuth angle (degrees)
θ_{3dB}	3 dB antenna beamwidth
λ	RF wavelength of transmitted signal (m)
Λ	Ocean wavelength (m)
ϕ	Wind direction with-respect-to radar line-of-sight
σ°	Normalised mean backscattering coefficient (dB)
σ_m°	Normalised median backscattering coefficient (dB)
A_e	Effective area of aperture
δA_c	Area of resolution cell
f	frequency
G	Antenna gain at centre of main-lobe
h	Sea water depth (meter)
H	Radar altitude (meter)
k_o	Radar wavenumber ($\frac{2\pi}{\lambda}$)
K	Sea wavenumber ($\frac{2\pi}{\Lambda}$)
R	Range (meter)
$W(K)$	1-D Sea Ripple Spectrum
$W(K, \phi)$	2-D Sea Ripple Spectrum

DSTO-TR-0945

1 Introduction

The limiting factor affecting the performance of most airborne radar systems in detecting targets on or near the wind-swept surface of the sea is return echoes from the sea surface known as sea clutter. One of the goals in this study is to develop a quantitative understanding of microwave scattering from the open ocean and from site-specific coastal land areas for medium- and high-PRF airborne surveillance radar systems operating in the L-band wavelengths. Altitude and sidelobe returns from sea and coastal land clutter play important roles in determining the minimum signal-to-clutter plus noise ratio and clutter-to-noise ratio to derive the required antenna sidelobe levels and probability of detection [25]. It is therefore, important to study the backscatter from the sea surface and coastal land areas for a wide-range of radar grazing angles, in particular returns from short-range, near-normal incidence angle [21]. This report evaluates clutter returns from a maritime environment for airborne surveillance L-band VV-polarised radar system for a wide range of grazing angles ($0.1^\circ < \psi < 90^\circ$), radar look directions, varying sea conditions and site-specific coastal land areas.

The concepts of microwave scattering theory of slightly rough surface have been applied to study the backscattering from sea surface for L-band VV-polarisation under standard atmospheric conditions [16, 14]. This allows us to formulate a second-order composite sea clutter model or *MCSM* in short, to predict the normalised sea backscattering coefficient, σ° , for varying sea conditions. Based on the two-scale sea surface model proposed by Guinard and Daley [16] and surface scattering model proposed by Fung and Lee [14], the *MCSM* sea clutter model takes into account polarisation, wind speed, azimuth and grazing angles variations. In this model, the backscattering coefficient, σ° , can be represented as the sum of separate contributions from specular return and resonant Bragg-scattering.

In the report, we also briefly review three commonly used semi-empirical sea clutter models. They are the Georgia Institute of Technology (GIT), the Hybrid (HYB), and the Technology Service Corporation (TSC) sea clutter models. These sea clutter models are collated with five sets of measured L-band VV-polarised data. Of the five data sets used, three sets of calibrated airborne L-band data were collected by the Naval Research Laboratory (NRL) in the late 60s and early 70s from several sea locations and in varying sea conditions. The fourth set of data was compiled by Nathanson and the updated sea backscattered coefficient values were published in his most recent book [29]. The last set of data was obtained from measured L-band VV-polarised polarimetric synthetic aperture radar (POLSAR) images of the Darwin region. These images were acquired during the PACRIM mission by the Jet Propulsion Laboratory on the 23rd November 1996.

For a radar system operating close to the coastal region, its detection and tracking capabilities will be severely affected by compounded backscatter from the coastal water, foreshore vegetation, and man-made structures. The clutter returns from the coastal areas will depend on the coastal terrain characteristics e.g., vegetation type, presence of man-made structures, ground surface roughness and many more [18, 30]. The availability of the Darwin POLSAR data allows us to study the characteristics of backscatter signals from coastal water, coastal saline flat surfaces and mangrove forest, and their dependence on grazing angle for an L-band VV-polarised radar system. Terrain scatterer types in the POLSAR images were identified using the TOPO-100K and TOPO-50K maps.

2 Backscattering from the Sea Surface in Standard Atmospheric Conditions (σ°)

The magnitude of the radar signal backscatter from the sea surface is dependent on a number of parameters; these include the wavelength of the transmitted microwave signal, the incidence or grazing angle, the polarisation of the transmitted wave, the reflective index of the sea surface, possible surface atmospheric effect such as surface and evaporation ducts, and environmental conditions (sea state and wind speed).

2.1 Dependence on Radar Grazing Angle

Studies observing, modelling and predicting the backscattering coefficients, σ° , from sea surface are probably the most extensive research aspect of radar sea return. One of the main factors affecting signal returns from the sea surface is the grazing angle of the transmitted wave. The range of possible grazing angles can be stratified into three distinct regions as shown in Figure 2.1 [29, 25]:

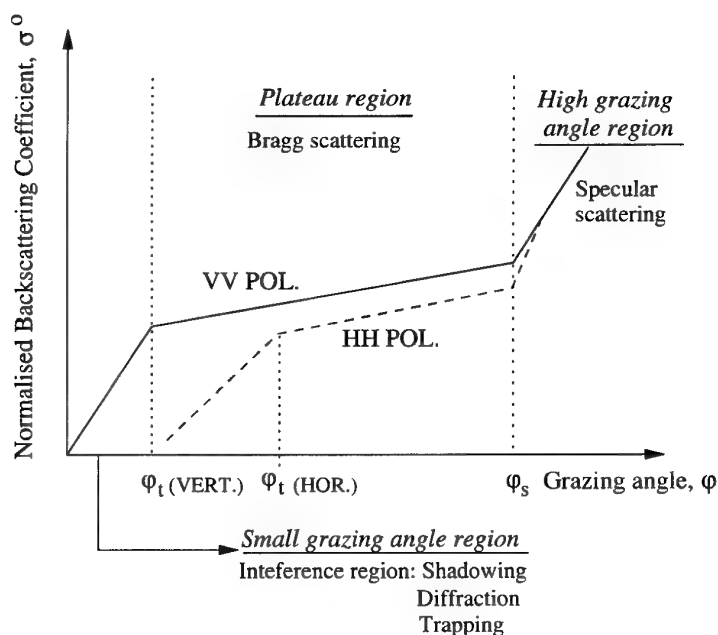


Figure 2.1: Relationship between grazing angle, polarisation and radar sea backscatter returns

1. *high-grazing-angle region* (quasi-specular) for grazing angle between ψ_s to 90° , $\psi \in [\psi_s, 90^\circ)$;

In the high-grazing-angle region, the magnitude of the backscatter signal from sea surface is controlled by mirror-like reflection of the local flat sea surface facets tilted to align normally to the incident signal.

2. *plateau-grazing-angle region* for grazing angle between critical angle to ψ_s , $\psi \in [\psi_t, \psi_s]$;

The magnitude of the backscatter signal from the sea surface is controlled by the Bragg resonant scatterers.

3. *low-grazing-angle region* for grazing angle below the critical angle, $\psi < \psi_t$;

Breaking waves, wedge scattering, multipath reflections and the presence of ducting significantly increase the backscatter signal.

The critical angle is [26]

$$\sin \psi_t = \frac{\lambda}{4\pi h_e} \quad (1)$$

where h_e is the RMS wave height. Note that the boundaries between the three regions change with wavelength, polarisation, and surface condition [22].

2.1.1 Quasi-Specular Grazing Angle Region

In the quasi-specular region, the magnitude of the backscatter signal is controlled by the mirror-like reflection of local flat facets tilted by the long gravity waves [23, 50]. Local surface waves tilted normal to the radar signal cause large specular returns for grazing angles near normal incidence.

$$\sigma^\circ = \underbrace{\sigma_S^\circ}_{\text{Specular Returns}} \quad (2)$$

The main contributor to the specular returns are the long gravity waves [13].

2.1.2 Plateau or Bragg Backscattering Region

The radar signal backscatter from the sea surface for grazing angles, $\psi_t \leq \psi < \psi_s$, at L-band is predominantly due to ocean waves with wave length similar to the transmitted wavelength. Known as *Bragg scatterers* or *Bragg's resonant ripples*, these water waves (half the radar wavelength) are the main source of backscattering for radar operating at grazing angle, ψ between 25° and 75° [42, 13, 44, 4]. The relationship between Bragg's resonant sea (or spatial) wavelength and transmitted wavelength is

$$\Lambda = \frac{\lambda}{2 \cos \psi} \quad (3)$$

where Λ is the sea wavelength, λ is the transmitted wavelength, and ψ is the local grazing angle. Lee and associates [20] studied the Bragg scatterers in detail and concluded that Bragg scatter is a single-bounce return in the absent of depolarisation and with negligible cross polarisation. Note that the Bragg resonant wavelength, Λ , is shorter at smaller grazing angle. The sea wavenumber is

$$K = \frac{2\pi}{\Lambda} \quad (4)$$

The first-order Bragg scattering mechanism for L-band radar falls in the *short gravity-capillary waves* region at midrange grazing angles in the absence of longer and higher gravity waves.

These short gravity-capillary waves provide the mechanism for microwave backscattering by forming distributed facets atop the gently undulating long *gravity waves* to reflect the signal back to the radar system. The long gravity waves have four significant effects on the short waves: (1) tilting the scattering surface, thereby, modifying the local grazing angle [16, 38] as shown in Figure 2.2; (2) local straining, causing amplitude variation over

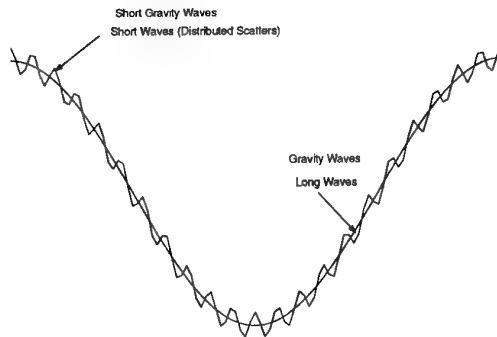


Figure 2.2: Two-scale Sea Surface

the longer wave, with maximum straining occurring near the crest of the gravity wave [38]; (3) advection by the orbital velocity of the gravity wave [38]; and (4) variation in radar range phase path [38].

2.1.3 Low Grazing Angle Region

At small grazing angles, the sea surface appears in the electromagnetic sense to be smooth for an L-band radar. There are a number of scattering mechanisms that contribute to the radar return signal from the sea surface at low grazing angles, in particular, breaking waves due to the large gravity waves, the effects of ducting, multipath reflection, and wedge scattering.

“Wedge scattering” is the scattering contribution from sea surface with small radius of curvature relative to the radar wavelength [24]. Lyzenga and associates [24] proposed an analytic expression to consider the contribution of wedge scattering to the sea surface backscattering coefficient, σ° .

$$\sigma_{VV-wedge}^\circ = \frac{g^2 L N}{\pi} \quad (5)$$

where N is the number of wedge crests per unit area and L is their average length. However, it has also been noted by the authors that they are unsure how these quantities can be measured accurately.

2.2 Dependence on Wind Speed

The σ° variation of the sea surface is dependent on the wind speed. The relation is however complex and uncertain. In early publications, Valenzuela and associates [46] have noted that the wind dependence of the sea spectrum is identical to the wind dependence of the σ° of the sea. Using the NRL-4FR data, Valenzuela [46] concluded that the σ° is less sensitive at L-band to increasing wind speed and the relationship is best approximated by a power law. Similarly, Daley [7] and Wetzel [39] have noted that the relationship between σ° from sea and wind speed for L-band is given by a power-law of the form

$$\sigma^\circ \approx U^{2\nu} \quad (6)$$

where the estimated values of 2ν from the NRL-4FR data [7] is

$$2\nu = \begin{cases} 0.4, & \text{Upwind} \\ 0.2, & \text{Downwind} \\ -0.1, & \text{Crosswind} \end{cases} \quad (7)$$

Similarly, Daley [9] has reported that the measured σ° (JOSS I data) is consistent with the power law described by Valenzuela [46]. Thompson and associates [41] have also reported the wind-speed exponent to be approximately, $2\nu = 0.5$. These data indicate a dependence upon surface wind speed since the L-band backscatter signal is approximately proportional to the square root of the wind speed.

However Donelan and Pierson [13] have argued that the power-law relationship underestimates the backscatter for high wind speed and overestimates the backscatter at low wind speed. They have shown that the high-wave number gravity-capillary waves is a function of both the wind speed and viscosity (variation of viscosity of sea water with temperature and salinity).

In addition, they have also proposed a threshold wind speed, whereby no backscattering in the plateau region (mid-range incidence angles) is observed below the threshold, and that this threshold speed is a function of the incidence angle and the sea water temperature. This minimum wind speed is required to overcome viscosity damping and allow the short gravity-capillary waves to grow [34]. At L-band for 30°C sea water temperature and $\psi = 70^\circ$, Bragg resonant backscattering is observed when the wind exceeds 1.7 m/s. At $\psi = 25^\circ$, it only need to exceeds 1.61 m/s [13].

The data reported by Morris [26] in Figure 2.3 shows that for VV polarised sea clutter, there appears to be little dependence on wind speed for grazing angles in the low and plateau regions. However, a slight dependence on wind speed is observed from HH polarised sea clutter at low grazing angles.

We can conclude that in L-band (VV polarisation), the backscatter from the sea surface has the following behaviour:

1. The radar backscatter, σ° , from sea increases slightly with increasing wind speed.
2. Wind dependence increases with decreasing grazing angle, and at near normal incidence, the backscatter is inversely proportional to wind speed [14, 19].

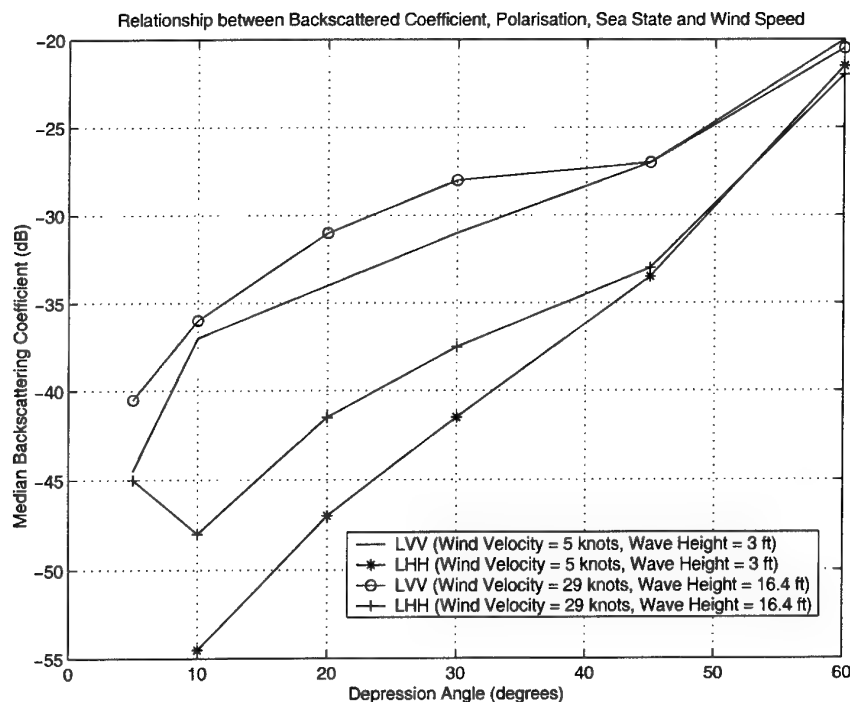


Figure 2.3: Dependence of σ_m° on Wind Speed, Wave Height and Polarisation [26]

2.3 Dependence on Wind Direction

The results published from several trials have shown that the backscattered signal from the sea surface is dependent on a factor that combines both the wind magnitude with its relative direction to the boresight. The sea clutter is strongest when viewed in the upwind direction, intermediate in the downwind direction, and weakest in the crosswind direction for S, X, and Ku-band sea clutter [39].

However, for an L-band radar, the sea surface appears smooth, resulting in negligible difference between upwind, and downwind backscatter returns [14]. Similar findings were reported by Chan [4] and Thompson and associates [41] for L-band radar. Chan found that the upwind/downwind ratio of σ° was close to unity, and the $\frac{\sigma_{VV}^\circ}{\sigma_{HH}^\circ}$ is very high for radar operating within these frequency bands. Thompson and associates [41] found little or no dependence of L-band backscatter on wind direction for stable atmospheric conditions, but observed that a strong dependence on wind direction occurred during unstable conditions.

2.4 Dependence on Rain

Rain does not produce an overriding influence with measurement of backscatter characteristics of sea surface for L-band radar [50]. In addition, studies have shown that the VV-polarised sea surface backscatter is insensitive to rain rate [39].

3 Data Source for L Band

Five sets of measured L-band VV-polarised data have been used to test the accuracy of the *GIT*, *HYB*, *TSC* and the proposed *MCSM* sea clutter models in predicting sea backscattering values for varying sea conditions and grazing angles. Measured sea backscattered signals on which analyses in this report are based on are: (1) Naval Research Laboratory (NRL) Four-Frequency radar (4FR) [46, 9] calibrated measurements; (2) measurements compiled by Nathanson [29]; and (3) Jet Propulsion Laboratory POLSAR Darwin data. Brief descriptions of the NRL 4FR sets of data, Nathanson's data and the DARWIN POLSAR data are summarised below.

3.1 Naval Research Laboratory Airborne Trials [46, 16, 8, 9]

Measurements of the normalised median radar backscattering coefficient, σ_m^0 , from the sea surface for varying grazing angles and sea conditions were recorded by the Naval Research Laboratory (NRL) in the 60s and early 70s [39, 8, 9]. The NRL deployment utilised an airborne system equipped with a four-frequency (4FR) radar system, transmitting a sequence of frequencies alternately in horizontal and vertical polarisation. The carrier frequencies were: (1) UHF (428 MHz); (2) L-band (1.228 GHz); (3) C-band (4.455 GHz), and (4) X-band (8.910 GHz). The system was calibrated against standard metal spheres, and measurements were recorded for upwind, downwind, and crosswind in wind speeds ranging from 5 to 50 knots (up to 7-8 m wave height), and over grazing angles ranging from 5° to 90°. Corresponding wind speeds and wave heights were recorded in the measurements areas from instrumented ships [39, 8, 9].

1. NRL-4FR Data [46]

Sea backscattered measurements recorded using the NRL 4FR radar system, off New Jersey in December 1964, off Puerto Rico in July 1965 and in the North Atlantic in February 1969 were considered in this report. Surface truth information for the Puerto Rico deployment was measured by a team of researchers from the Applied Physics Laboratory, John Hopkins University, in an instrumented vessel [16]. For the North Atlantic deployment, the surface truth information was provided by oceanographic surface vessels operated by the French and British governments [16]. We will hereafter refer the data measured as the NRL-4FR data.

2. Joint Ocean Surface Study, 1970 (JOSS I) [9]

The NRL 4FR system was employed by the Naval Oceanographic Office in January 1970 to measure calibrated sea backscattered signals for various sea states, radar wavelength, polarisation, and depression angle off the vicinity of Argus Island, Bermuda.

The 4FR system was operating at a pulse width of 0.5 μ s, PRF of 683 Hz, IF bandwidth of 10 MHz, and range-gate width of 24 ns. Surface truth information was acquired utilising an altimeter and aerial cameras [9]. Wind and wave height information were recorded by observers stationed on Argus Island.

3. Joint Ocean Surface Study, 1971 (JOSS II) [10]

The NRL 4FR system was employed by the Naval Oceanographic Office in February 1971 to measure calibrated sea backscattered signals for various sea states, radar wavelength, polarisation, and depression angle off the East Coast of Northern America.

Surface truth data was acquired at the site of study from an instrumented buoy and an ocean station vessel. Wind velocity, direction, and average wave height information were obtained hourly from both of these instruments [10]. The values of the 4FR system used during the JOSS II program were PRF, 512 Hz; pulse width, 1.0 μ s; IF bandwidth, 10 MHz; and range-gate width, 24 ns [10].

For all analyses carried out in this report, the median sea backscattered values were converted to mean values assuming an exponentially distribution or Rayleigh in amplitude [39].

3.2 Normalised Mean Backscattering Coefficient (σ°) compiled by Nathanson [29]

Nathanson compiled measurements of the sea surface normalised mean backscattering coefficient, σ° , given the sea state, polarisation, and carrier frequency from approximately 60 experiments. Some of the values tabulated in his most recent book [29] were approximated by extrapolation and interpolation between points or were averaged of upwind, downwind, and crosswind situations. Grazing angles were adjusted from depression or incidence angles, and in some data, median values were adjusted to mean values.

Some general comments about the database:

- (a) Measurements were collected from L-band radar systems operating at pulse widths ranging from 0.5- to 5- μ s.
- (b) The database contains many uncertainties at low carrier frequencies and low grazing angles.
- (c) Nathanson believed that the σ° values reported for low grazing angles to be higher than true mean values due to the following:
 - (i) Early data were generated from less sensitive radar and values reported were only of data above normal (above known mean values), and from unknown wind speed, sea state, and ducting conditions;
 - (ii) The high occurrence of ducting increases the σ° values at very low grazing angles.
- (d) Although the mean values published in his most recent book represent lower σ° values than that reported in 1969, they might still be higher than true mean values due to ducting conditions.

Although the data compiled by Nathanson is biased above the true mean values, it nevertheless provides the upper limit scenario when evaluating the radar performance in average sea conditions.

3.3 POLSAR Darwin Data

POLSAR is a NASA-sponsored polarimetric synthetic aperture radar system developed at the Jet Propulsion Laboratory in California. The POLSAR system provides high quality polarimetric SAR data in three frequencies; P ($\lambda = 67.0$ cm, $f = 0.44$ GHz), L ($\lambda = 23.9$ cm, $f = 1.25$ GHz) and C ($\lambda = 5.6$ cm, $f = 5.39$ GHz) bands in four transmit/receive polarisation (VV, HH, VH, HV).

3.3.1 Study Area

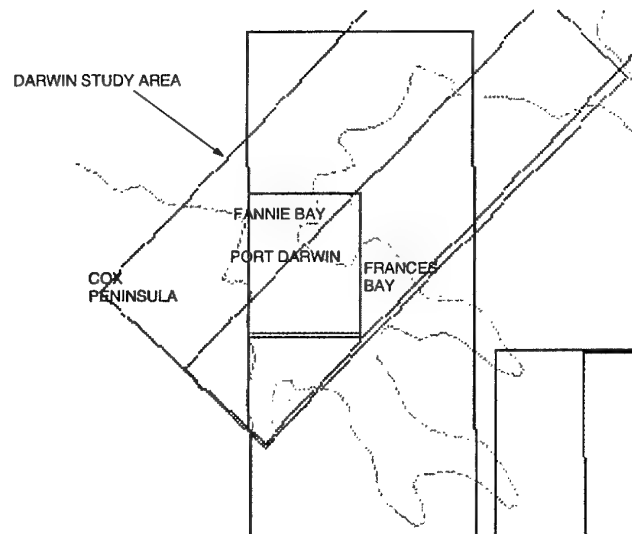


Figure 3.1: Location of the Study Area

The study area of interest was conducted in the Darwin region ($130^{\circ} 45' E$, $12^{\circ} 30' S$) located in the Northern Territory of Australia (Figure 3.1). The monsoon season in this region falls between December and March, with average rainfall of approximately 1624 mm [3]. The daily maximum temperature ranges between $30^{\circ}C$ to $34^{\circ}C$ (hottest months are November and December), and the minimum temperature ranges between $19^{\circ}C$ to $27^{\circ}C$ (coolest month is July) [3].

The study area consists of several land cover classes, but only vegetation close to the coastal region is considered in this report. The Northern Territory coast can be seen as an heterogeneous evergreen mangrove forest covering an area of $4,120 \text{ km}^2$ [3]. The mangrove forest of the Northern Territory forms a distinct lineal growth along the shorelines of the coastal regions. Mangrove community patterns surrounding the coastal areas of Darwin, with a total extent of 20,4000 hectares is dominated by *Ceriops tagal* forest as shown in Figure 3.3 (a). The height of these trees ranges from 1 to 10 meters and very often homogeneous population of this tree type can be found in the mid and high tidal flat regions and in the hinterland regions, covering 40% of the mangrove forest areas (Figure 3.2). Soil composition in these regions are generally muds and sandy muds.

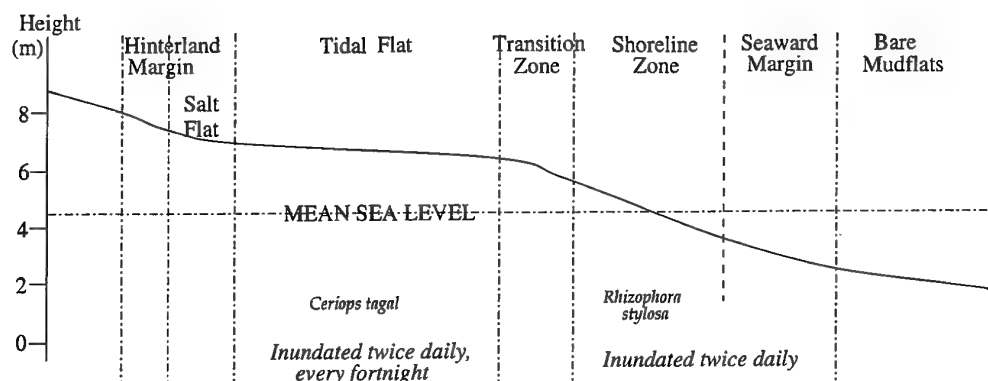


Figure 3.2: Zonation of Mangroves - Darwin Harbour [3]



Figure 3.3: (a) *Ceriops tagal* low closed-forest (mid tidal flat), and (b) *Rhizophora stylosa* closed-forest/low closed-forest (shoreline forest) [3]

Rhizophora stylosa closed-forest is also commonly found along the tidal creeks and the seaward fringes of the main tidal flat [3], varying in height from 6 to 18 meters (covering approximately 33% of the mangrove areas). As shown in Figure 3.3 (b), these trees generally have straight single bole in the tallest stumps with aerial root structure forming dense entanglement visible during low-tide. The height of these mangrove trees decreases as we move towards a higher tidal level. It has been noted that the mangrove vegetation of the above two species are particularly sensitive to cyclonic activities common in the Northern Territory. Defoliation and high mortality is observed following this disturbance [3], resulting in a different signature of backscatter characteristics observed by the radar system. Mud flats on the seaward margin are generally devoid of vegetation below the 3 m tidal level [3].

The JPL POLSAR system was flown over the study site onboard a DC-8 on the 23rd November 1996. Two flight passes were selected and the two L-band polarimetric SAR images of vertical (VV) polarisation collected with bandwidth of 40 MHz are shown in Figure 3.4 and 3.5.

The POLSAR data were processed as a 60km strip image by the JPL's Radar Data

Center using version 6.10 (CM5512 - Figure 3.4) and 5.10 (CM5148 -Figure 3.5) integrated processor. The number of looks processed in the azimuth is 18 and 1 in range.

Table 3.1: POLSAR Specifications for the 23 November 1996 Darwin Deployment

Description	CM5512	CM5148
Acquisition Time (GMT)	17378.0	16746.0
Frequency (GHz)	1.218	1.218
Near Slant Range (m)	9013.26	9013.26
Far Slant Range (m)	17537.36	19244.51
Near Look Angle (θ_i)	22.5°	22.6°
Far Look Angle (θ_i)	61.7°	61.7°
Range Resolution (m)	3.3310	3.3310
Azimuth Resolution (m)	9.2592	9.2592
Image Size (pixels)	4183 × 2560	1095 × 2560

Limited ground truth is available for vegetation measurements of the site of interest. However, detail ground truthing of moored vessels, sea and meteorological conditions were conducted by a team of DSTO scientists. On the 23rd November 1996, moored vessels were photographed and position recorded at the Fannie Bay (by Mr David Clark) and Port Darwin (by Dr. Ed Kruzins) areas. At the same time, aerial photographs of the POLSAR swath area were obtained from an altitude of 26,000 ft. with the assistance of the local coastwatch personnel. Two passes of the Darwin harbour were conducted by Mr Kim Meaney: (1) an approximately east-west pass; and (2) an approximately north-south pass. Long focal lenses of 600mm and 1200mm were used to ground truth moored vessels in the Darwin harbour (look angle to targets is approximately 45°). In addition, a 4 ft. square corner reflector was placed in an open area at the northern end of the Darwin airport. Recorded measurements of the sea and meteorological conditions are tabulated in Table 3.2.

Table 3.2: Hydro-meteor Parameters for the 23 November 1996 Darwin Deployment (Provided by Dr. Ed Kruzins, DSTO)

Description	Darwin Harbour	Fannie Bay
Acquisition Time (CST)	12:17 pm	10:40 am
Air Temperature (Dry)	35.0°C	32.5°C
Air Temperature (Wet)	29.0°C	27.0°C
Relative Humidity	68%	64%
Cloud Cover	5/8 Octa	3/8 Octa
Cloud Type	Cirrus/Cumulus	Cirrus and Strato-Cumulus
Wind Speed	14 km/h	4 kt
Wind Direction	170°	SE
Wave Height	1 cm	Calm

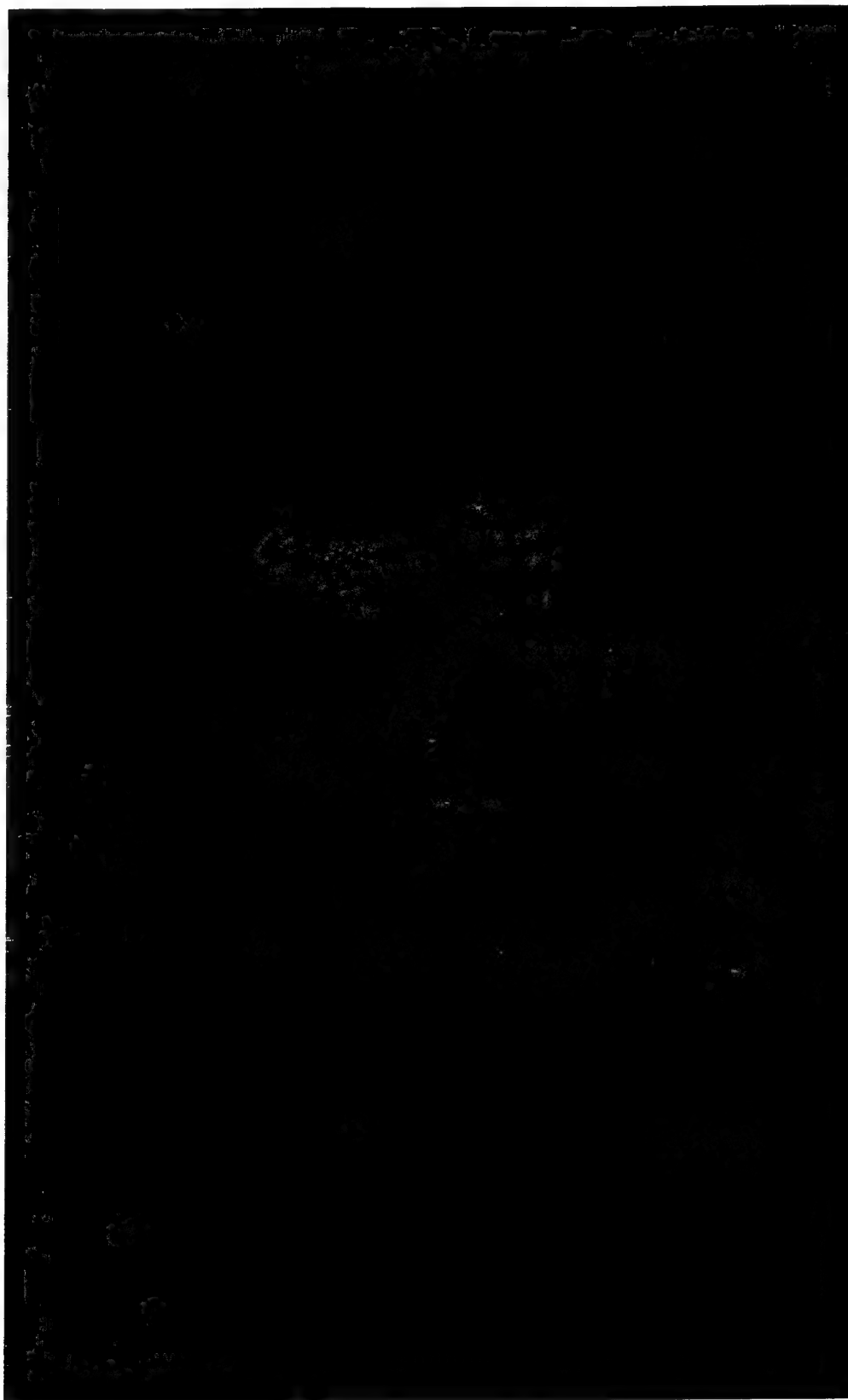


Figure 3.4: POLSAR Darwin L-band VV data (CM5512)



Figure 3.5: POLSAR Darwin L-band VV data (CM5148)

3.3.2 SAR Terrain Analysis Program

A program has been written in MATLAB to analyse the JPL POLSAR images. The main user interface is shown in Figure 3.6.



Figure 3.6: SAR Analysis GUI Interface

A number of flexible options have been incorporated into the software design. These options allow the user to specify the near and far slant ranges, radar altitude, and near and far field directions. In addition, for high resolution data or images, the user is able to view the image in sub-quadrant (maximum of 4).

The program allows the user to operate in two modes:

1. Pixel Mode

In the pixel mode, a dialog box pops-up allowing the user to view the backscattering coefficients, σ° , of individual pixel and grazing angle at the mouse position. An example of the dialog box is shown below (Figure 3.7).

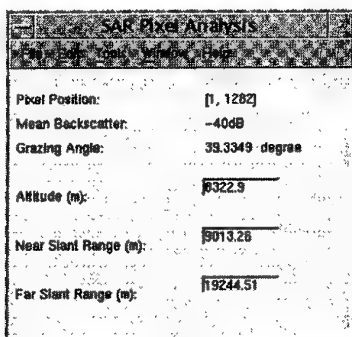


Figure 3.7: SAR Pixel Analysis GUI Interface

2. Area Mode

(a) Segment Profile

The segment profile mode allows the user to specify a line segment of the image of interest using a mouse. The program calculates the grazing angle and normalised backscattering coefficient, σ° , for every pixel on the line segment.

(b) Area Profile

The area profile mode allows the user to crop a small area of the image to determine a set of backscattering coefficient, σ° , with its corresponding grazing angle value. Provisions have also been made to allow the user to view the histogram of σ° of the selected area, and save the measured values to a file.

Radar backscattered signals from the sea surface were extracted from the CM5512 and CM5148 POLSAR images around the Port Darwin area at a distance away from the coastal saline flat surfaces. Figure 3.8 shows the σ° as a function of grazing angle.

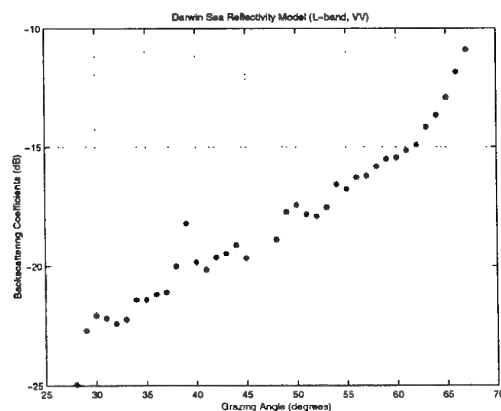


Figure 3.8: Normalised σ° coefficients from the sea surface (L-VV, $U = 3.88$ m/s)

4 Semi-Empirical Sea Clutter Models

There are a number of established semi-empirical sea clutter models available for determining the sea backscattering coefficient, σ° , given knowledge of the radar parameters, sea conditions, and method of observation. These models provide a fairly accurate estimation of the sea clutter backscattering coefficient, σ° . Three empirical sea clutter models suitable for determining the radar sea returns for L-band radar have been selected for further consideration in this report. The first model is derived from the *Georgia Institute of Technology (GIT)*, the second model is a *Hybrid (HYB)* model that include works from Barton [35], and the third model is derived from *Technology Service Corporation (TSC)* [1]. These three sea clutter models are applicable to a wide range of frequencies. However, the *GIT* ($0.1^\circ \leq \psi \leq 10^\circ$) and *HYB* ($0.1^\circ \leq \psi \leq 30^\circ$) models are applicable only to low-grazing angles, while the *TSC* ($0.1^\circ \leq \psi \leq 90^\circ$) model is applicable to a wide range of grazing angles [1].

The effectiveness of the *GIT*, *HYB*, and the *TSC* models in modelling sea clutter were compared with measured data under similar sea conditions. Radar sea clutter measurements are derived from: (1) NRL-4FR data [46, 8], and (2) σ° measurements compiled by Nathanson [29].

The *GIT*, *HYB* and *TSC* models are described below:

(a) Georgia Institute of Technology (GIT) Sea Clutter Model [37, 1]

The Georgia Institute of Technology Sea Clutter Model, hereinafter referred to as the *GIT* clutter model, is derived from multiple data sets observed under "standard" propagation conditions, and mathematical models of the various sea surface backscattering mechanism. The *GIT* sea clutter model describes the backscattering coefficient as a function of three factors: (1) Interference factor, G_m ; (2) sea condition - wind speed factor, G_u ; and (3) direction dependence - wind direction factor, G_w . The interference factor uses wave height to take into account the transition in receiver power from R^{-3} (plateau region) dependency to R^{-7} in the low-grazing angles [37]. This model is listed in Appendix B.1.

(b) Hybrid (HYB) Sea Clutter Model [35]

The hybrid model (HYB) is derived from information of the average sea clutter data compiled by Nathanson in 1969, works by Barton, and features of the *GIT* model [29]. The hybrid model is suitable for assessing the sea backscattered coefficient, σ° , for grazing angle between 0.1° and 30° . This model, hereinafter referred to as the *HYB* model, is listed in Appendix B.2.

(c) Technology Service Corporation (TSC) Sea Clutter Model [1]

The Technology Service Corporation sea clutter model, hereinafter referred to as the *TSC* sea clutter model, is an empirical model derived from Nathanson's average sea clutter data published in 1969. The *TSC* model assumes that the Nathanson's data is the average for all look directions, and hence treats it as cross-wind data. The *TSC* models takes into consideration the sea conditions such as Douglas sea states to compute wind speed and wave height.

It has been noted by Reilly [35] that the *TSC* model includes the effect of some ducting and hence predicts higher σ° at low-grazing angles. Dockery [12] suggested that in the absence of prior information about propagation conditions, the *TSC* model better represents average sea conditions [37, 12]. This model is listed in Appendix B.3.

A summary of the semi-empirical sea clutter capabilities is tabulated below [37, 1]:

Table 4.1: Semi-Empirical Sea Clutter Capabilities

Description	<i>GIT</i>	<i>HYB</i>	<i>TSC</i>
Frequency Band (GHz)	1-100	0.5 - 35	0.5 - 35
Sea Conditions	Wind Speed (m/s)	Douglas Sea States (0 - 5)	Douglas Sea States (0 - 5)
<i>Geometry</i>			
Grazing Angle ($^\circ$)	0.1 - 10	0.1 - 30	0.1 - 90
Aspect Angle ($^\circ$)	0 - 180	0 - 180	0 - 180
Polarisation	VV, HH	VV, HH	VV, HH

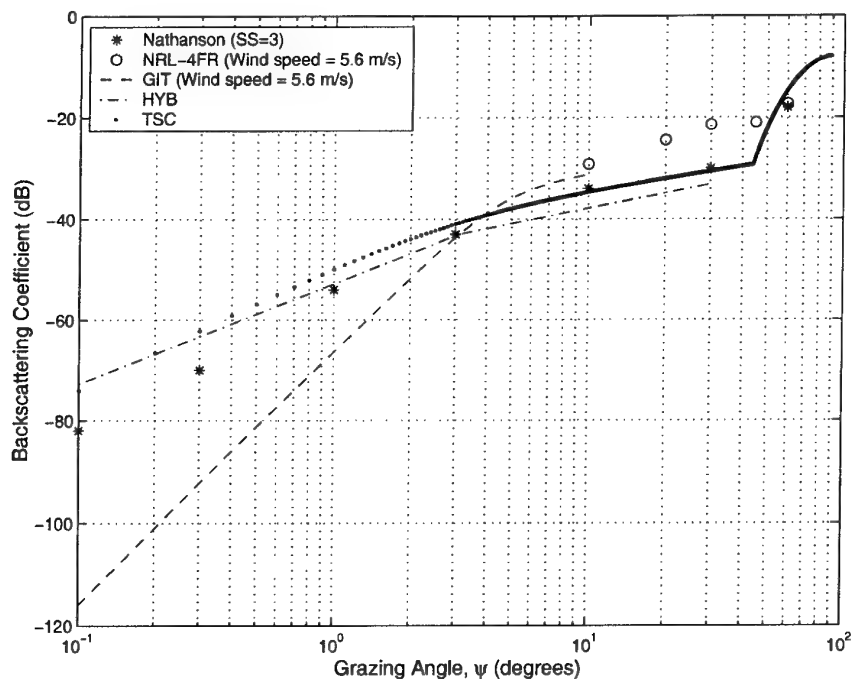
4.1 The Use of Nathanson and NRL-4FR Data Sets to Test the *GIT*, *HYB*, and *TSC* Models

The average backscattering values compiled by Nathanson and the NRL-4FR data sets have been used to test the accuracy of the *GIT*, *HYB*, and *TSC* sea clutter models. The plots of Figure 4.1 (a) and (b) compare these three sea clutter models at wind speed of 5.6 m/s and 12.1 m/s. These plots apply to an L-band radar with carrier frequency of 1.25 GHz with radar transmitting and receiving at vertical polarisation and an upwind radar azimuth direction.

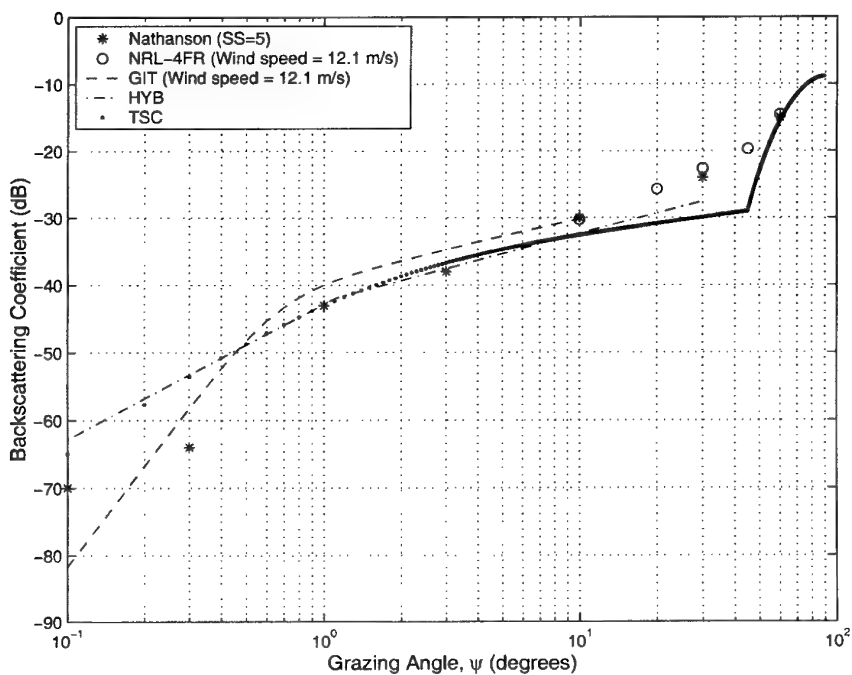
(a) Discussion on *GIT* Sea Clutter Model

The *GIT* model takes into account the multipath returns at low grazing angle. The multipath or interference factor, G_m , is a theoretically derived factor to account for multipath interference for Gaussian distributed wave heights [32]. Therefore, at small grazing angle, the *GIT* model, exhibits a rapid falloff at the rate of ψ^4 [35] as shown in Figure 4.1 (a) and (b). This small angle region is also known as the "Interference Region". However, this approach is justified only in the absence of ducting or other non-standard propagation effects [12]. The remaining two factors, G_u and G_w , were derived empirically to account for wind speed and wind direction variation, respectively.

When comparing the predicted σ° with the measured NRL-4FR and Nathanson's data, the *GIT* model has close agreement with both sets of data for $\psi > 1^\circ$. Since the NRL-4FR data is limited to grazing angle larger than 10° , it is difficult to evaluate the accuracy of the *GIT* model. However for grazing angle, $\psi < 1^\circ$, close agreement between Nathanson data and *GIT* predictions occurs only at higher wind speed



(a)



(b)

Figure 4.1: Comparisons of Semi-Empirical Sea Clutter Models at L-band (VV-Pol. and Upwind): (a) Wind speed = 5.6 m/s, and (b) Wind speed = 12.1 m/s.

(12.1 m/s) [refer to Figure 4.1 (b)]. Poor agreement can be seen in Figure 4.1 (a) for low surface wind speed. Large differences between the *GIT* model and Nathanson data may be attributed to the heavy averaging done by Nathanson [49, 32] on data measured under a wide variety of propagation conditions, and the selective recording of measured data.

One major drawback of the *GIT* models, is the limited range of grazing angles ($0.1^\circ \leq \psi \leq 10^\circ$). Since we are interested in determining the backscattered returns from sea clutter for grazing angles between $\psi = 0^\circ$ and $\psi = 90^\circ$, the *GIT* model is not suitable for our application.

(b) Discussion on *TSC* and *HYB* Sea Clutter Models

The *TSC* and *HYB* sea clutter models were derived by empirically fitting curves to large quantities of Nathanson's data, measured under a wide variety of propagation conditions [12]. The empirical parameters in the *TSC* and *HYB* models were adjusted using measured σ° to reduce the falloff at small grazing angles [35]. These models exhibit a ψ^2 falloff behaviour at low grazing angles [35]. As shown in Figure 4.1 (a) and (b), the sea backscattering coefficient, σ° , predicted by the *TSC* and *HYB* model is significantly higher than the corresponding *GIT* predictions for grazing angles less than 1° . These sea clutter models are in reasonable agreement, especially with Nathanson data for low wind speed (5.6 m/s), but deviate for higher wind speed (12.1 m/s) for $\psi < 1^\circ$.

At higher grazing angles ($\psi > 1^\circ$), differences between these models and Nathansons' data are significantly reduced. In the absence of sea ducting conditions, Dockery [12] suggested using the *HYB* or *TSC* model to represent the average propagation conditions. However, if propagation information is available, Dockery [12] suggested using a modified *GIT* model that explicitly includes the propagation factor (ducting or nonstandard atmospheric effects) to model the sea clutter. Using sea clutter measurements collected with a 2.9 GHz radar, upwind, and wind speed of 6.2 m/s, Dockery [12] showed that the modified *GIT* model is in reasonable agreement with the measured σ° compared with the *HYB* or the *GIT* models.

Poor agreement between the measured NRL-4FR data, and the predicted σ° values were observed in Figures 4.1 (a) and (b) for higher grazing angles ($\psi > 10^\circ$) for both wind speeds. Both sea clutter models underestimated the predicted backscattered coefficient, σ° , for both wind speeds. The discrepancy between the measured and predicted sea backscattered coefficients increases with increasing grazing angles and wind speeds. However, in the quasi-specular region ($\psi > 60^\circ$), there is good agreement between measured backscatter values and predicted *TSC* sea clutter values.

5 Composite Sea Clutter Models

The composite sea clutter models to be developed in the later sections are based upon the two-scale sea clutter model developed by Guinard and Dailey [16]. These models take into account polarisation, wind speed, and azimuth plus grazing angles variation.

The backscattering coefficient, σ° , from the sea surface can be represented as the sum of separate contributions from specular return and Bragg-scattering.

$$\sigma^\circ = \underbrace{\sigma_S^\circ}_{\text{Specular Returns}} + \underbrace{\sigma_B^\circ}_{\text{Bragg Scattering}} \quad (8)$$

The composite sea clutter model will be constructed based on these two forms of scattering mechanism. The primary scattering mechanism in the low-grazing angle and plateau regions is assumed to be Bragg scattering whereby the backscattering coefficient, σ_B° , is in proportion to the spectral density of the short gravity-capillary waves for a fully developed sea [13]. At near normal incidence, the effects of specular return, σ_S° , due to the stationary facet normal to the radar signal is included.

5.1 Specular Backscattering for Fully Developed Sea

Near-normal incidence backscatter from the sea surface is better described by the specular point or tilted facet model [44, 47]. The radar backscatter returns from the sea surface at near normal incidence is in proportion to the number of mini-facets normal to the incident ray. According to Barrick [2], specular return from the sea surface is valid only for grazing angles greater than 75° . For grazing angles less than 75° , the backscatter return is more diffuse and is best described by the Bragg diffraction model.

For an isotropic rough surface of Gaussian statistics, the normalised backscatter return at near normal incidence is [44]

$$\sigma_S^\circ = \frac{|R(0)|^2}{s^2} \sec^2 \theta_i \exp(-\tan^2 \theta_i / s^2) \quad (9)$$

where $R(0)$ is the Fresnel reflection coefficient of the sea surface at normal incidence, s^2 is the mean-square sea slope and θ_i is the angle of incidence.

Tilting of the sea surface due to the presence of swells or large gravity waves would cause the actual or local grazing angles to be different from those calculated from a flat sea surface assumption. Under the flat sea surface assumption, the relationship between the incidence angle and the grazing angle is

$$\psi = 90^\circ - \theta_i \quad (10)$$

If the sea surface is elevated, using the equivalent earth radius method, the local grazing angle as shown in Figure 5.1 is

$$\psi' = \psi + \theta_r \quad (11)$$

where θ_r is slope of the sea surface in the direction of the radar system.

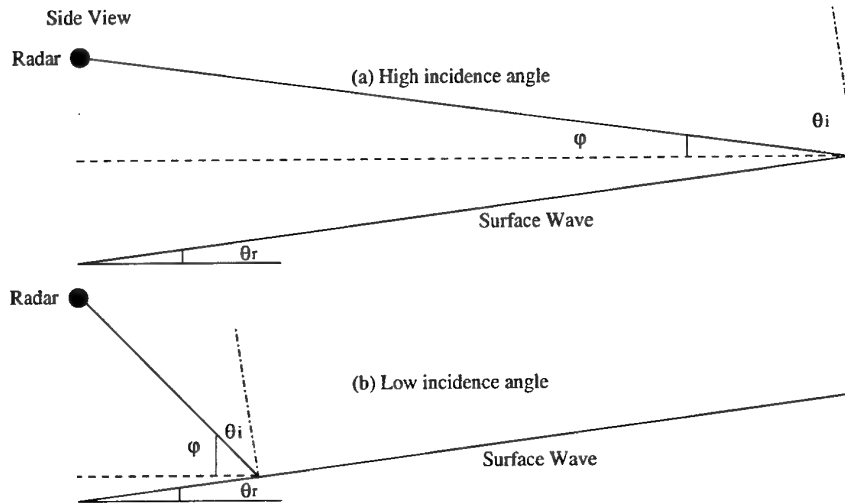


Figure 5.1: Grazing Angle Error due to Sea Surface Slope

The effect of the sea surface slope has a significant effect on the local grazing angles for high incidence radar look angles [refer to Figure 5.1 (a)]. However, for very low incidence radar look angles, the sea surface slope, θ_r , has small or negligible effects on the local grazing angles, ψ [refer to Figure 5.1 (b)].

In the composite sea clutter model, we did not take into account the correction to the local grazing angle due to sea surface slope when determining specular returns from the sea surface at near normal incidence angles.

(a) Mean-Square Sea Slope, s^2

The specular effect takes into account backscatter contribution from the large scale waves or the long gravity waves. The total mean-square sea slope, s_T^2 is described by two components: (1) crosswind (s_c^2), and (2) up/downwind (s_u^2); where both components are a function of wind speed, U [2]. An empirical model relating these to wind speed was determined from measurements obtained optically by Cox and Munk in 1954 [6].

For a clean sea surface,

$$\begin{aligned} s_c^2 &= 0.003 + 1.92 \times 10^{-3}U \pm 0.002 \\ s_u^2 &= 0.000 + 3.16 \times 10^{-3}U \pm 0.004 \\ s_T^2 = s_c^2 + s_u^2 &= 0.003 + 5.12 \times 10^{-3}U \pm 0.004 \end{aligned} \quad (12)$$

For an oil slick sea surface,

$$\begin{aligned} s_c^2 &= 0.003 + 0.84 \times 10^{-3}U \pm 0.002 \\ s_u^2 &= 0.005 + 0.78 \times 10^{-3}U \pm 0.002 \\ s_T^2 = s_c^2 + s_u^2 &= 0.008 + 1.56 \times 10^{-3}U \pm 0.004 \end{aligned} \quad (13)$$

where the \pm value gives the standard deviation of the observed value when computing the regression model.

Hence to determine the slope contribution of the long gravity waves only, it is necessary to remove contributions to s_c^2 and s_u^2 by the short gravity-capillary waves. It has also been noted by Valenzuela [44] that for sea backscattering away from normal incidence, only a proportion of the total mean-square slopes, s_T^2 of the sea surface is included in s^2 ($s^2 < s_T^2$), this being the contribution of long gravity waves in a fully developed sea whose wavelengths are greater than the radar L-band wavelength.

Cox and Munk [6] found that the oil slick sea surface tends to smooth out the contributions of the capillary waves. Therefore, the mean slope of the Cox and Munk oil slick sea surface model, s_c^2 and s_u^2 of Equation (13) would be a good approximation of the proportionate contribution of the total mean-square slope by the long gravity waves. Valenzuela [44] also obtained relatively good agreement with the NRL-4FR measured radar backscattered returns near normal incidence when the mean-square slopes for a sea with oil slick is used.

However, it has been noted by Donelan and Pierson [13] that using the long gravity waves spectrum to determine the required slope variances, s^2 has some shortcomings in low and high winds. The gravity waves on the sea are usually higher than the corresponding fully developed sea when winds are light and lower during high winds. Therefore, instead of the linear wind speed dependence, we are proposing the application of a differential relationship as follows [6]:

$$s^2 = \begin{cases} 5.12 \times 10^{-3}U, & U < 5\text{m/s} \\ 1.56 \times 10^{-3}U, & U \geq 5\text{m/s} \end{cases} \quad (14)$$

(b) Reflection Coefficients, $R(0)$

Daley and Barrick [44] found good agreement between measured sea returns at near-normal incidence and predicted σ_g^0 values using Equation (9). However, discrepancies between measured returns and predicted values were observed for incidence angles away from near-normal. To remedy this, Valenzuela suggested using the mean-square slopes derived for an oil slick sea surface and adjusting $|R(0)|$ as follows:

$$|R(0)| = \left| 0.52 \frac{\epsilon_r - 1}{(\sqrt{\epsilon_r} + 1)^2} \right| \quad (15)$$

where ϵ_r is the relative dielectric constant of sea water at L-band (1.275 GHz) [13]. Note that a constant 0.52 is used in Equation (15) instead of the proposed 0.65 by Valenzuela [44]. Better agreement between predicted backscatter values, σ_g^0 , and measured L-band JOSH I backscatter values were observed when using the composite sea clutter model with a constant of 0.52.

5.2 Two-Scale Bragg Model

For grazing angles less than 75° , the Bragg diffraction model best describes the diffuse backscatter from micro-facets or short gravity-capillary waves [2]. Guinard and Daley [16] proposed a composite sea surface scattering model based upon the resonant scattering theory of the sea surface. The composite sea clutter model was derived to remove the constraints of the small perturbation method that the product of the vertical component

of the wave number and the surface displacement must be small. The composite sea surface model is based upon a two-scale model in which a slightly rough surface (short gravity-capillary waves) is superimposed on a larger wave structure (long gravity waves). The short gravity-capillary wave with wave number, $K = 2k_o \sin \theta_i$ forms the facets for radar backscattering (also termed Bragg scatterers), while the longer waves modulate the Bragg scatterers by "tilting" or changing the local incidence angle [16].

However, it has been observed by Valenzuela and associates [46] that, the backscattered sea clutter for vertical polarisation is insensitive to the tilting effect. Therefore for practical purposes, the backscatter signal for vertical polarisation sea clutter can be predicted by slightly rough surface scattering theory with no modification to the radar depression angle except to account for diffraction due to non-homogeneous atmospheric medium.

5.2.1 First-Order Composite Sea Clutter Model (CSM), $\sigma_{B^1(pp)}^\circ$

The composite sea clutter model, hereinafter referred to as the *CSM* sea clutter model is a two-part first-order model, whereby the scattering from any composite rough sea surface whose wave length is Bragg resonant and height is given by Phillips' proposed equilibrium range spectrum [16].

$$\begin{aligned} \text{Horizontal Polarisation, } \sigma_{B^1(HH)}^\circ &= 4\pi k_o^4 \sin^4 \psi \alpha_{HH} \underbrace{W(K_x, K_y)}_{\text{Surface Height Spectrum}} \\ \text{Vertical Polarisation, } \sigma_{B^1(VV)}^\circ &= 4\pi k_o^4 \sin^4 \psi \alpha_{VV} \underbrace{W(K_x, K_y)}_{\text{Surface Height Spectrum}} \end{aligned} \quad (16)$$

where k_o is the radar wave number, ψ is the grazing angle, and K_x, K_y are the wave numbers in the x and y directions on the infinite surface [16].

Philips found that at equilibrium range, the L-band sea spectrum has the form

$$W(K) \approx BK^{-4} \quad (17)$$

where $K = \sqrt{K_x^2 + K_y^2}$ and $B = 6 \times 10^{-3}$ for gravity waves.

The CSM model for an L-band radar system could therefore be simplified to the following:

$$\begin{aligned} \text{Horizontal Polarisation, } \sigma_{B^1(HH)}^\circ &= 1.5 \times 10^{-3} \pi \alpha_{HH} \tan^4 \psi \\ \text{Vertical Polarisation, } \sigma_{B^1(VV)}^\circ &= 1.5 \times 10^{-3} \pi \alpha_{VV} \tan^4 \psi \end{aligned} \quad (18)$$

where ψ is the local grazing angle.

The first-order scattering coefficient, α_{pp} is [16]

$$\begin{aligned} \text{Horizontal Polarisation, } \alpha_{HH} &= \frac{(\epsilon_r - 1)}{[\cos \theta_i + \sqrt{(\epsilon_r - \sin^2 \theta_i)}]^2} \\ \text{Vertical Polarisation, } \alpha_{VV} &= \frac{(\epsilon_r - 1)[\epsilon_r(1 + \sin^2 \theta_i) - \sin^2 \theta_i]}{[\epsilon_r \cos \theta_i + \sqrt{(\epsilon_r - \sin^2 \theta_i)}]^2} \end{aligned} \quad (19)$$

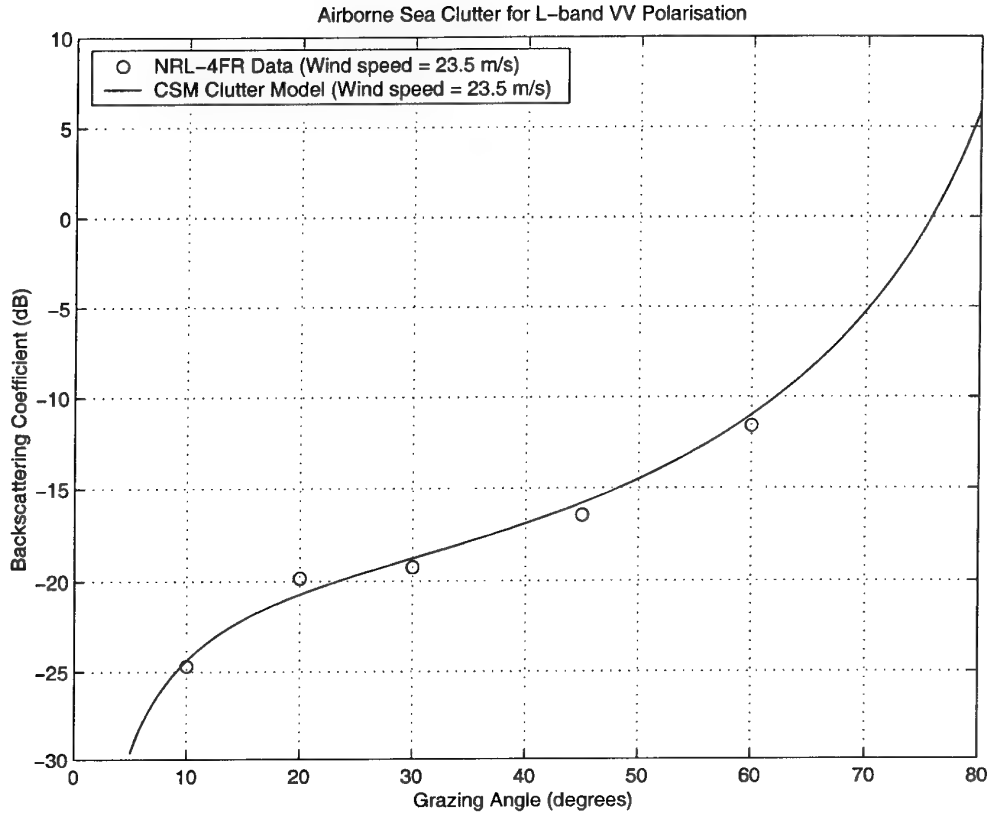


Figure 5.2: CSM L-band Sea Clutter Model (1.228 GHz) [16]

where ϵ_r is the relative dielectric constant of the sea surface with value $72 - j59$ at L-band (1.275 GHz) [13].

A comparison of the CSM sea clutter model with the NRL-4FR data recorded in the upwind direction with sea surface wind speed of 24 m/s and swell of 8 meters is shown in Figure 5.2:

1. The CSM model provides a realistic upper bound for VV-polarisation data for grazing angle, $\psi < 75^\circ$;
2. To the first order, $\sigma_{B1(VV)}^\circ$ is given by the spectral density of the resonant Bragg waves [51].

The CSM sea clutter model estimates the backscattering from the sea surface under saturation conditions. The model assumes the spectral density of the resonant Bragg wave to be independent of wind speed under saturation conditions [33]. As shown in Figure 5.2, the CSM sea clutter model provides a realistic sea clutter model for high sea state conditions, e.g., for wind speed of 23.5 m/s which according to Nathanson [29] is categorised as *strong gale* condition. However, a more appropriate sea clutter model responsive to wind speed changes is required to evaluate the sea backscattering coefficient, σ° , for various sea conditions.

5.2.2 Second-Order Composite Sea Clutter Model (*MCSM*)

The original *CSM* model was modified into a three-part, second-order sea clutter model and hereafter referred to as the *Modified Composite Sea Clutter* model or *MCSM* in short. The *MCSM* sea clutter model is based upon the concept of slightly rough sea surface scattering whose length is Bragg resonant and height is given by a second-order directional sea spectrum proposed by Fung [14] and Chen [5]. The model also accounts for specular return near-normal incidence

MCSM Modified Sea Clutter Model

Reflectivity equation (dB m²/m²),

$$\sigma^{\circ} = \sigma_S^{\circ} + \sigma_{B^2(pp)}^{\circ} \quad (20)$$

1. Second Order Bragg Scattering Model, $\sigma_{B^2(pp)}^{\circ}$

$$\begin{aligned} \text{Horizontal Polarisation, } \sigma_{B^2(HH)}^{\circ} &= k_o^2 \sin^4 \psi \alpha_{HH} \underbrace{W(K, \phi)}_{\text{Directional Sea Spectrum}} \\ \text{Vertical Polarisation, } \sigma_{B^2(VV)}^{\circ} &= k_o^2 \sin^4 \psi \alpha_{VV} \underbrace{W(K, \phi)}_{\text{Directional Sea Spectrum}} \end{aligned} \quad (21)$$

where k_o is the radar wavenumber, ψ is the grazing angle, K is the sea wavenumber, and ϕ is the wind direction with respect to boresight.

2. The first-order scattering coefficient, α_{pp} is [16]

$$\begin{aligned} \text{Horizontal Polarisation, } \alpha_{HH} &= \frac{(\epsilon_r - 1)}{[\cos \theta_i + \sqrt{(\epsilon_r - \sin^2 \theta_i)}]^2} \\ \text{Vertical Polarisation, } \alpha_{VV} &= \frac{(\epsilon_r - 1)[\epsilon_r(1 + \sin^2 \theta_i) - \sin^2 \theta_i]}{[\epsilon_r \cos \theta_i + \sqrt{(\epsilon_r - \sin^2 \theta_i)}]^2} \end{aligned} \quad (22)$$

where ϵ_r is the relative dielectric constant of the sea surface with value $72 - j59$ (L-band, 1.275 GHz) [13].

3. Two-dimensional (2-D) Sea Ripple Spectrum

Adopting the 2-D sea ripple spectrum developed by Pierson [43] and modified by Fung and Lee [5], the 2-D directional (taking into account the wind direction) sea spectrum is [43, 5]

$$W(K, \phi) = \frac{1}{2\pi} (1 + r \cos 2\phi) W(K) \quad (23)$$

(a) The constant, r , is given by

$$r = 2 \frac{(1 - \nu)}{(1 + \nu)}$$

where ν is the ratio of the slope variances in the *crosswind* and *upwind* directions [15, 43, 5],

$$\nu = \frac{s_c^2}{s_u^2} = \begin{cases} \frac{0.003 + 1.92 \times 10^{-3} U}{3.16 \times 10^{-3} U}, & U < 5 \text{ m/s} \\ \frac{0.003 + 0.84 \times 10^{-3} U}{0.005 + 0.78 \times 10^{-3} U}, & U \geq 5 \text{ m/s} \end{cases}$$

and U (m/s) is the wind speed at an altitude of 12.5 m above the sea surface.

(b) Wind Direction, ϕ

$$\text{Wind direction, } \phi = \begin{cases} 0^\circ, & \text{upwind} \\ 90^\circ \text{ or } -90^\circ, & \text{crosswind} \\ 180^\circ, & \text{downwind} \end{cases}$$

(c) 1-D sea ripple spectra for a single wave train, $W(K)$ [15, 43, 5]

$$W(K) = A(2\pi)^{p-1} \frac{\left(1 + 3 \frac{K^2}{K_m^2}\right) g^{\frac{(1-p)}{2}}}{K^{0.922} \left[K \left(1 + \frac{K^2}{K_M^2}\right)\right]^{\frac{(1+p)}{2}}} \quad (24)$$

where $A = 1.75$ if $U < 5$ m/s or $A = 0.875$ if $U \geq 5$ m/s, $K_m^2 = \frac{2\rho}{\tau} = (3.63)^2 \text{ cm}^{-2}$, g = acceleration of gravity 9.81 m/s^2 , ρ = sea water density, and τ = sea surface tension. Note that according to Valenzuela [45], K should have a -3.922 power law rather than the usual -4 law for L-band resonant Bragg waves. This has been adopted in the *MCSM* model.

According to Fung [15] and Chen [5] the relationship between the sea surface wind speed at an altitude z and friction velocity at neutral stability of the atmosphere, U^* is [17]

$$U = \frac{U^*}{0.4} \ln \left(\frac{z}{Z_0} \right)$$

where

$$Z_0(\text{cm}) = \left(\frac{0.684}{U^*} \right) + 4.28 \times 10^{-5} U^{*2} - 0.0443$$

and $p = 5 - \log_{10} U^*$.

5.2.3 The Use of the NRL-4FR Data to Test the CSM and MCSM Models

To check the validity of the models, we compared the *CSM* and *MCSM* backscatter predictions with the NRL-4FR data [46]. Plots of the predicted and measured upwind backscattering coefficients, σ° , versus grazing angles for varying sea surface wind conditions are shown in Figures 5.3 (a) - (e).

The plots of Figures 5.3 (a) - (e), show a slight increase in σ° with an increase in wind speed. Good agreement between predicted backscatter values and measured data is observed for intermediate upwind wind speed, $5 < \text{wind speed} < 20$ m/s for the *MCSM* sea clutter model. However, the *CSM* model overestimates the backscattering coefficients, σ° , for upwind speed within this intermediate range. A similar result is observed for very low wind speed (2.5 m/s) but good agreement between predicted *CSM* values and measured data is observed for very high wind speed (23 m/s).

At very low wind speed (2.5 m/s), the *MCSM* model also over-estimates the upwind backscattering coefficient, σ° , for low grazing angles, but good agreement is observed at higher grazing angles. However, the opposite is observed at very high surface wind speed condition (23.5 m/s). Disagreement between the predicted *MCSM* and measured values becomes evident at higher grazing angles for very high wind speed (23.5 m/s).

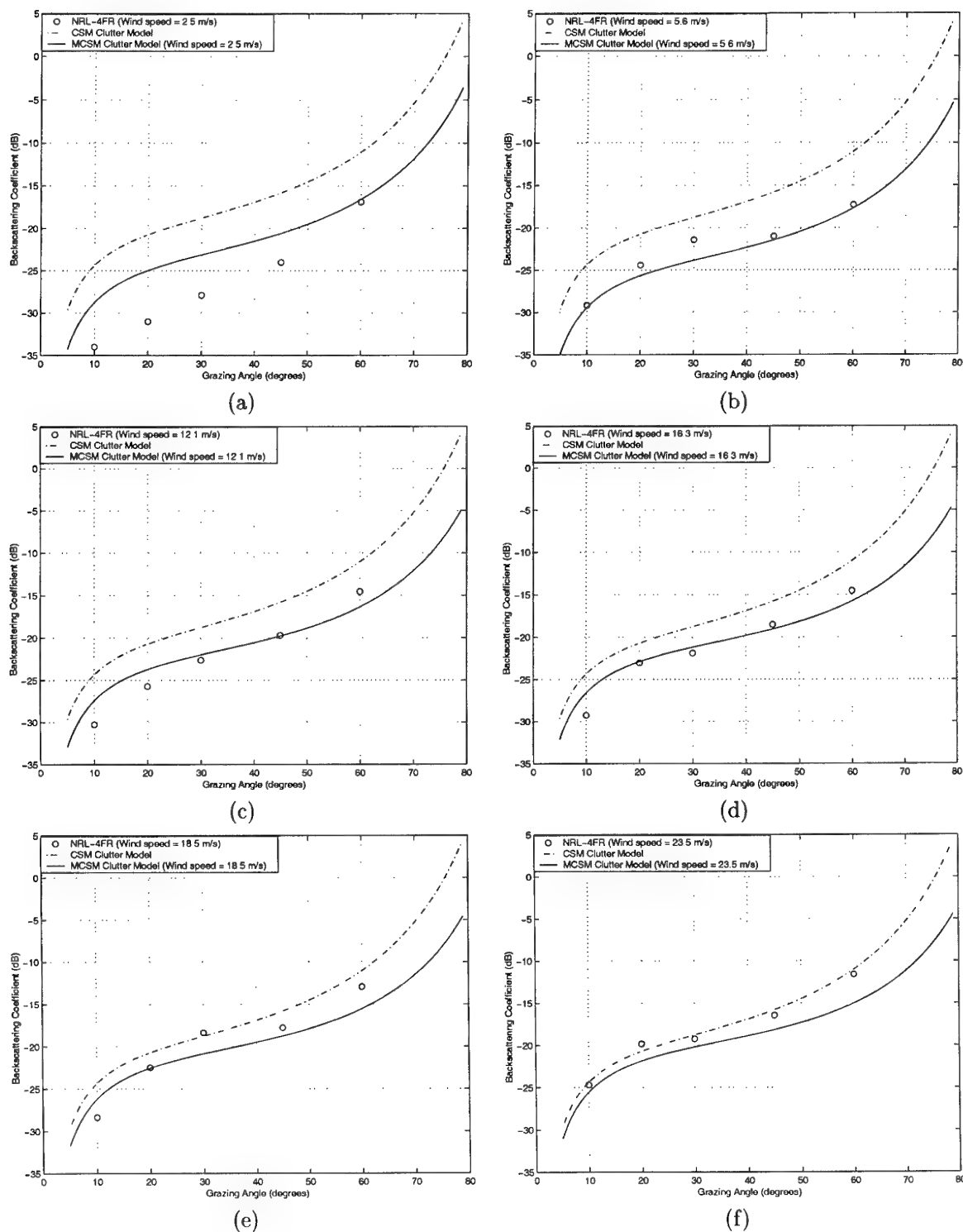


Figure 5.3: Dependence of σ^0 on wind speed, U (L-band, VV-Pol. and upwind). (a) wind speed = 2.5 m/s; (b) wind speed = 5.6 m/s; (c) wind speed = 12.1 m/s; (d) wind speed = 16.3 m/s; (e) wind speed = 18.5 m/s; and (f) wind speed = 23.5 m/s

6 Comparisons with Radar Measurements

As discussed earlier in Section 4.1, poor agreement between the *TSC* and *HYB* sea clutter models and the measured NRL-4FR data were observed for two wind speeds (5.6 m/s and 12.1 m/s). We revisited the exercise of testing the accuracy of these semi-empirical models with the same measured NRL-4FR data, but this time we included the *MCSM* model in the exercise.

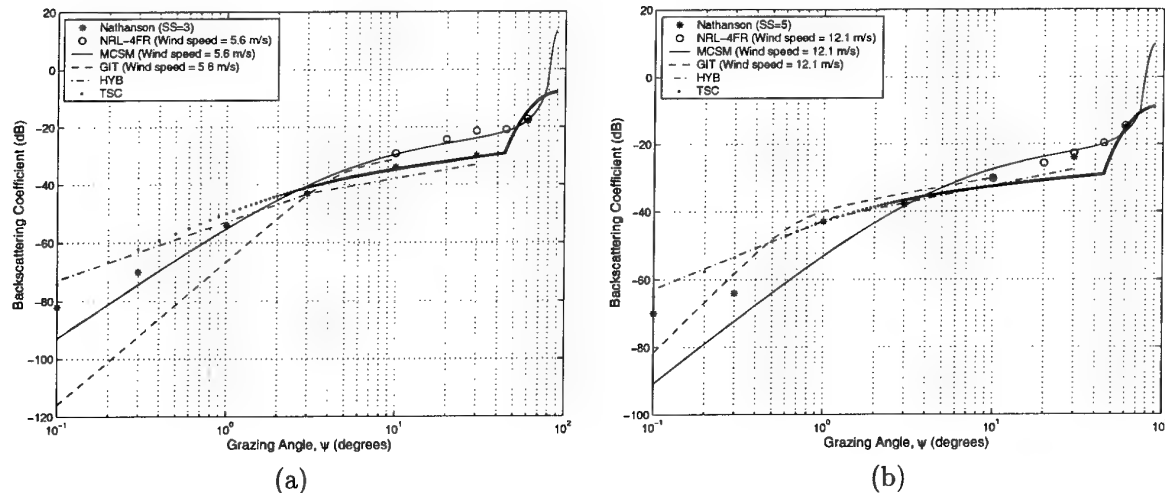


Figure 6.1: Dependence of σ_m° on Wind Speed, V_w (L-band, VV-Pol. and Upwind). (a) Wind speed = 5.6 m/s; (b) Wind speed = 12.1 m/s;

Plots of the results in Figures 6.1 (a) and (b) show good agreement between the measured NRL-4FR data and the *MCSM* predicted σ° values for $\psi > 3^\circ$ for the two wind speeds. For $\psi < 3^\circ$, good agreement between Nathanson's averaged data and *MCSM* predicted σ° values occurs at low wind speed (5.6 m/s), but discrepancies occur at higher wind speed (12.1 m/s).

We further tested the validity of the *MCSM* sea clutter model in predicting L-band V-pol. sea clutter under varying sea conditions using the JOSH I, JOSS II, and the POLSAR DARWIN measured data. Figures 6.2 - 6.4 (a) - (d) again show the poor agreement between the *TSC* and *HYB* models with the JOSS I measured data for varying wind speeds and radar look directions. Where these two models fail, the *MCSM* shows good agreement with the measured data for all wind speeds, radar look directions and grazing angles. Similar results were observed with the JOSS II measured data, shown in Figures 6.5 - 6.7 (a) - (c).

For the POLSAR data acquired over the DARWIN region under low wind speed condition, the *MCSM* model again accurately predicted the backscattering coefficients, σ° , for $20^\circ < \psi < 65^\circ$. Figure 6.8 shows the measured data, and the predicted σ° values by the *MCSM* and *TSC* sea clutter models. The *TSC* model underestimates the backscatter values when compared to the measured data.

We have tested four sea clutter models against measured data obtained from calibrated

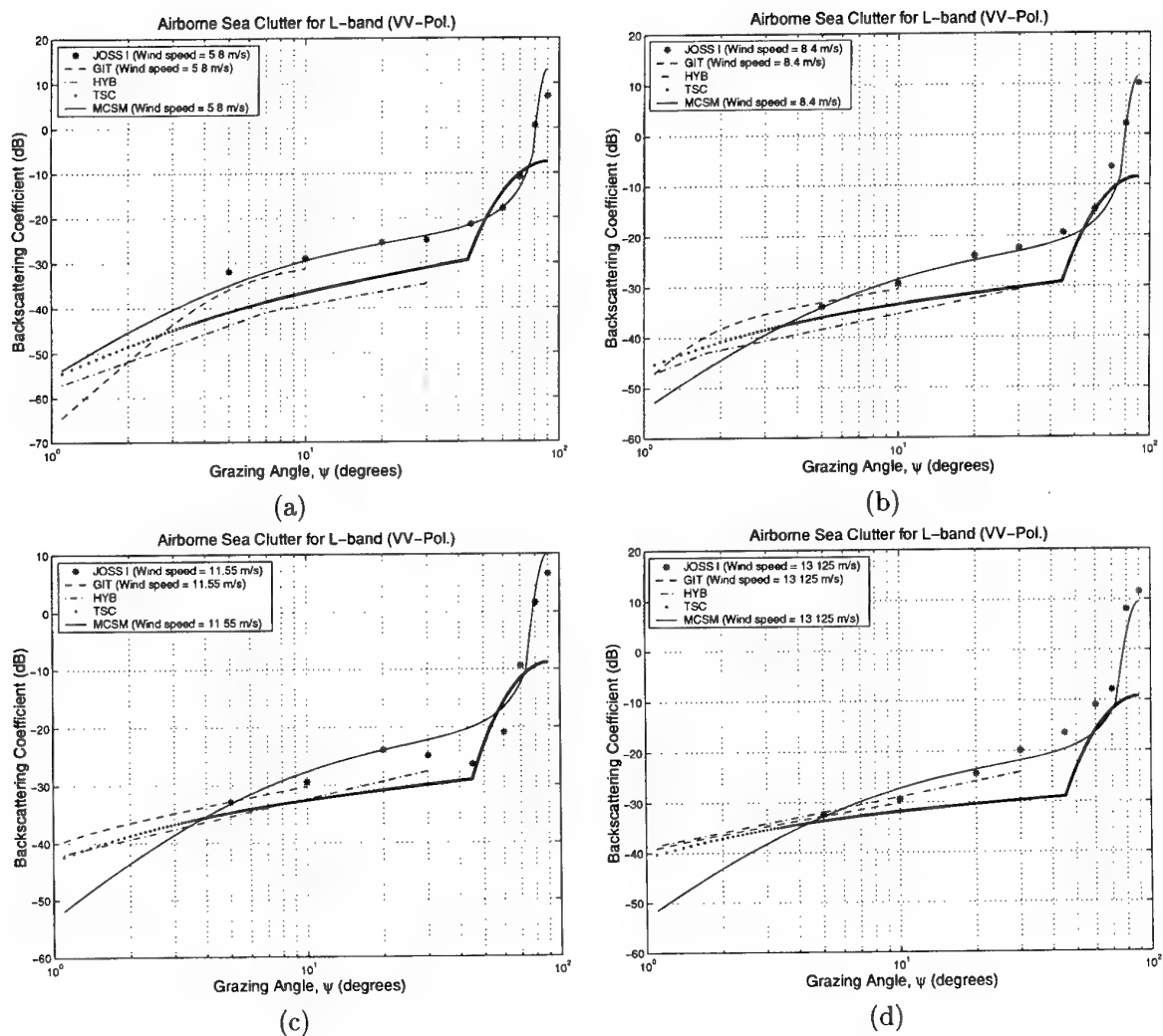


Figure 6.2: Dependence of σ^0 on wind speed - JOSH I, U (L-band, VV-Pol. and upwind).
 (a) wind speed = 5.8 m/s; (b) wind speed = 8.4 m/s; (c) wind speed = 11.55 m/s; (d)
 wind speed = 13.125 m/s

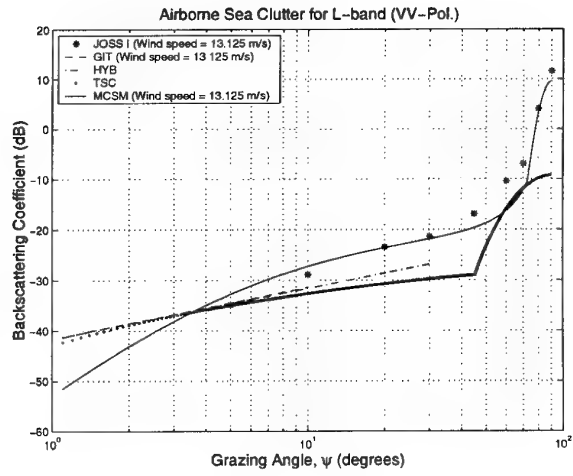
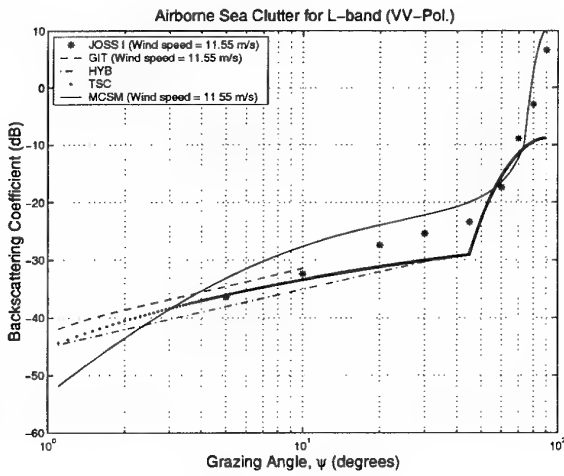
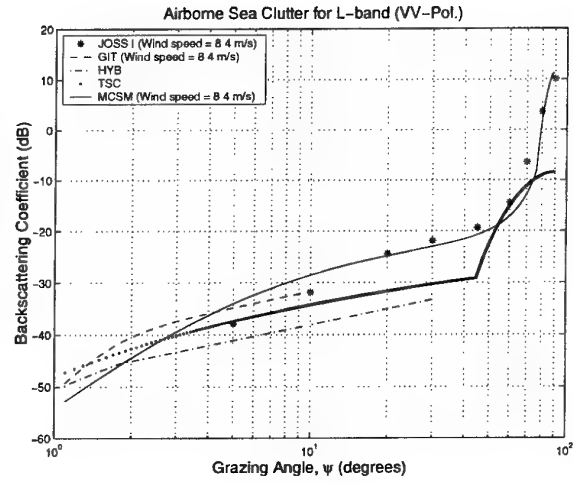
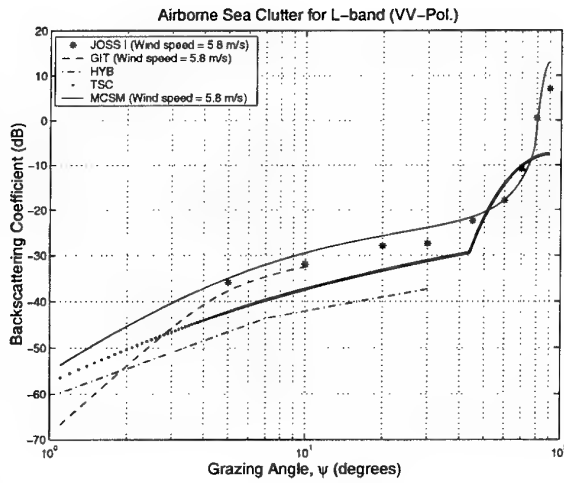


Figure 6.3: Dependence of σ^0 on wind speed - JOSH I, U (L-band, VV-Pol. and down-wind). (a) wind speed = 5.8 m/s; (b) wind speed = 8.4 m/s; (c) wind speed = 11.55 m/s; (d) wind speed = 13.125 m/s

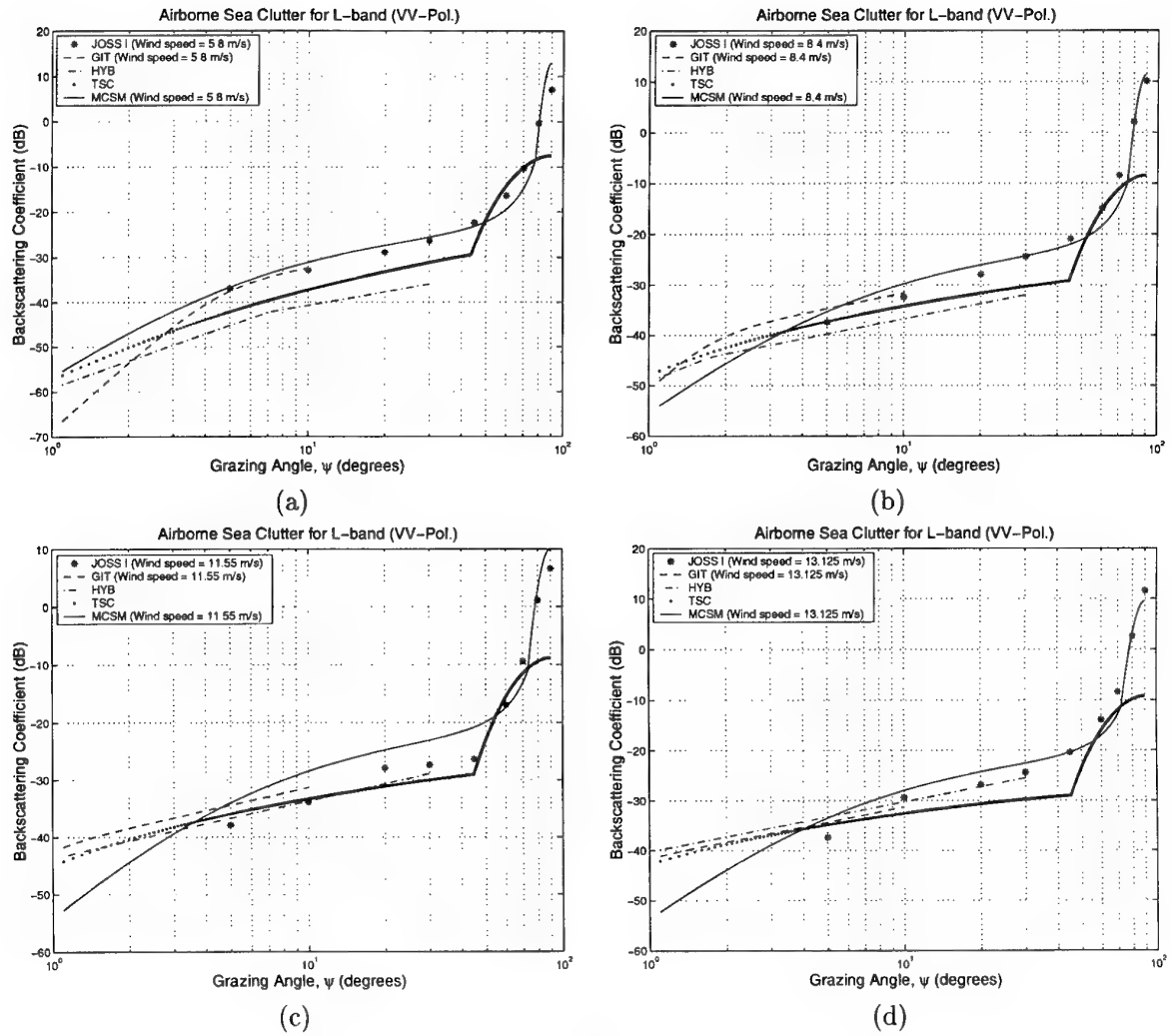
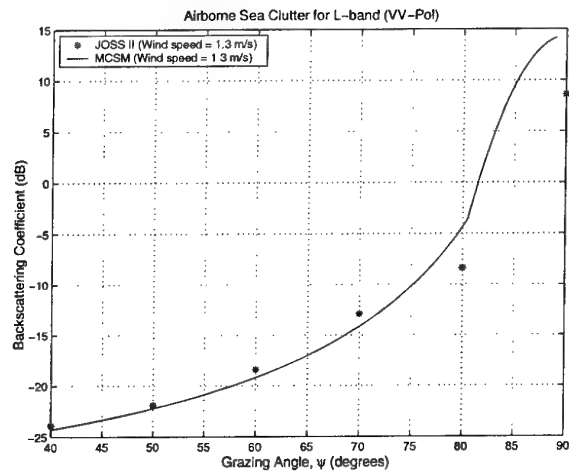
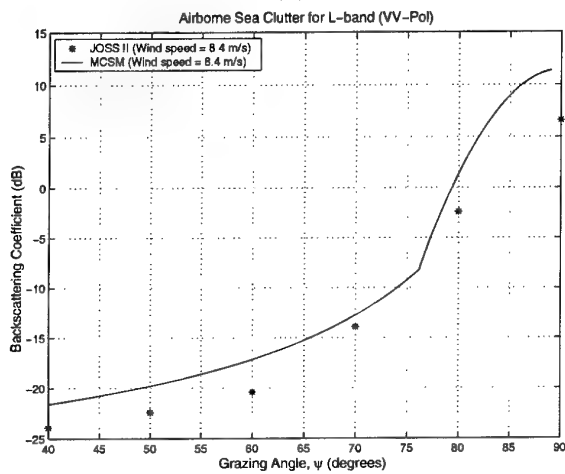


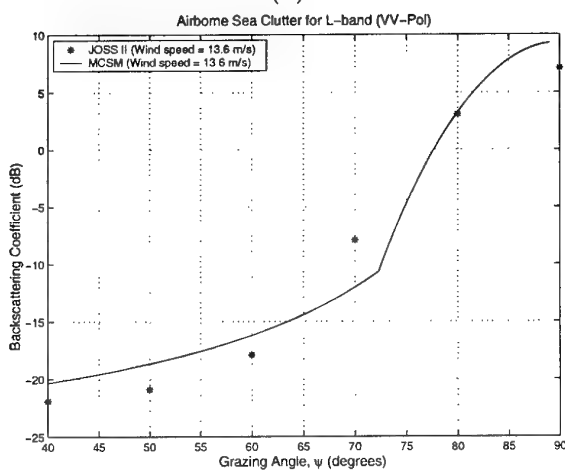
Figure 6.4: Dependence of σ° on wind speed - JOSH I, U (L-band, VV-Pol. and cross-wind). (a) wind speed = 5.8 m/s; (b) wind speed = 8.4 m/s; (c) wind speed = 11.55 m/s; (d) wind speed = 13.125 m/s



(a)



(b)



(c)

Figure 6.5: Dependence of σ^0 on wind speed - JOSH II, U (L-band, VV-Pol. and upwind).
 (a) wind speed = 1.3125 m/s; (b) wind speed = 8.4 m/s; (c) wind speed = 13.6 m/s

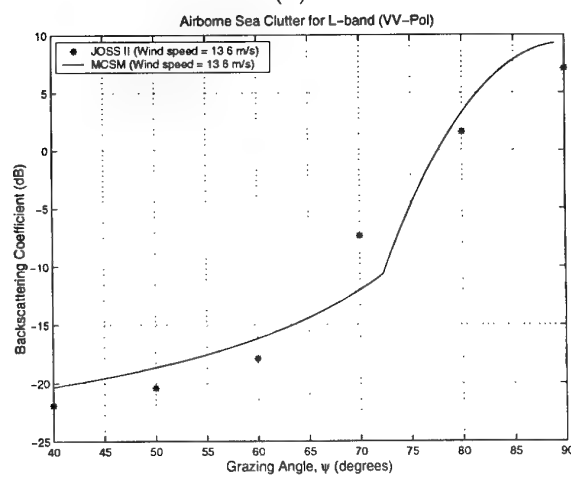
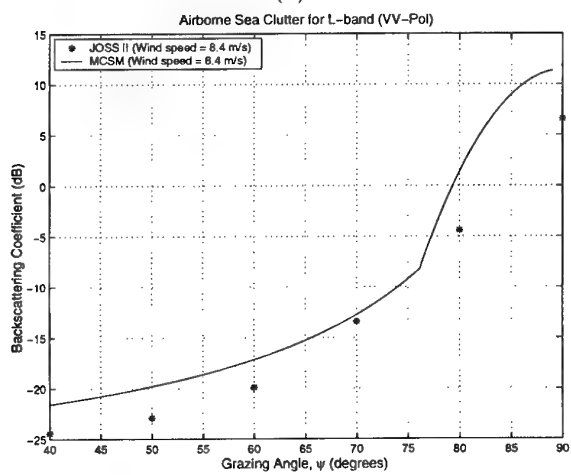
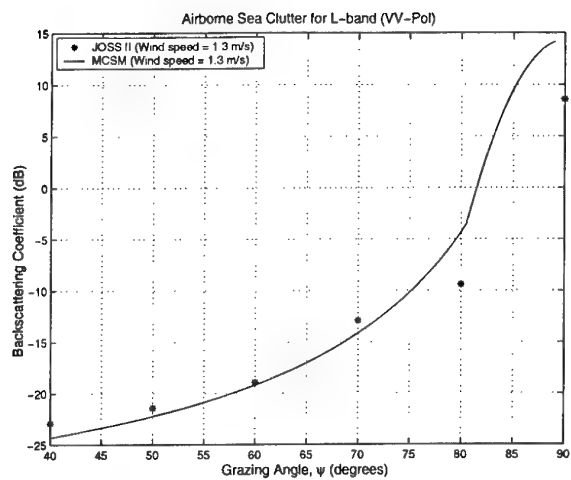


Figure 6.6: Dependence of σ^0 on wind speed - JOSH II, U (L-band, VV-Pol. and down-wind). (a) wind speed = 1.3125 m/s; (b) wind speed = 8.4 m/s; (c) wind speed = 13.6 m/s

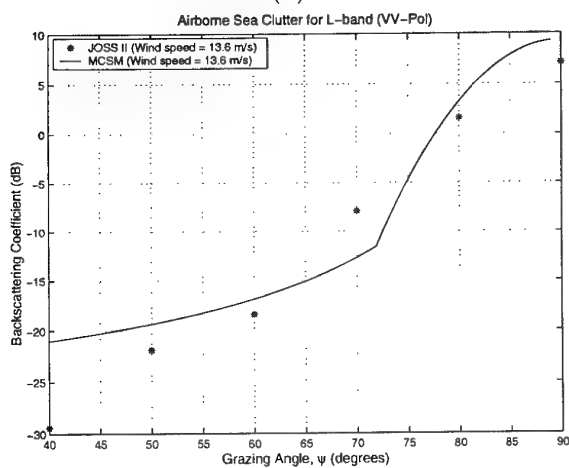
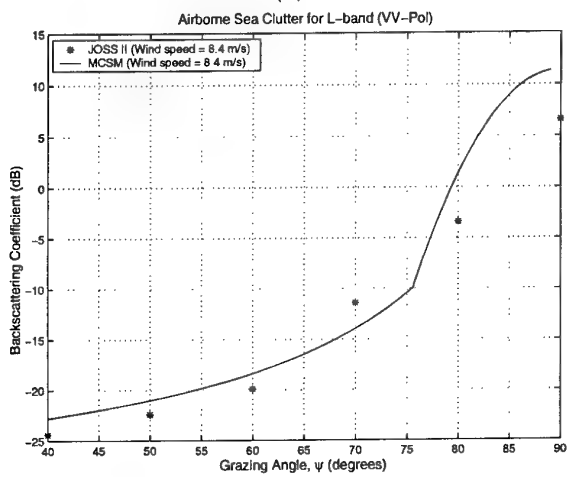
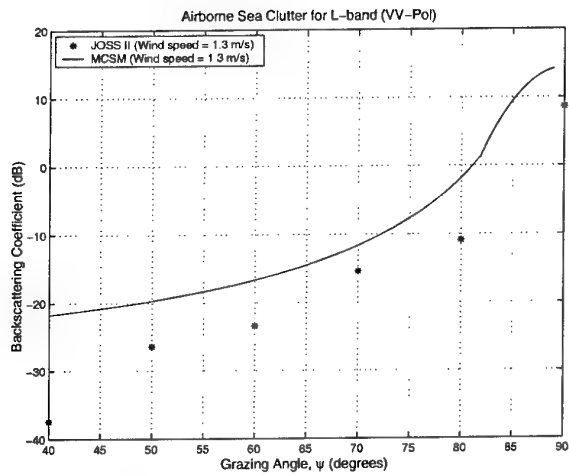


Figure 6.7: Dependence of σ^0 on wind speed - JOSH II, U (L-band, VV-Pol. and cross-wind). (a) wind speed = 1.3125 m/s; (b) wind speed = 8.4 m/s; (c) wind speed = 13.6 m/s

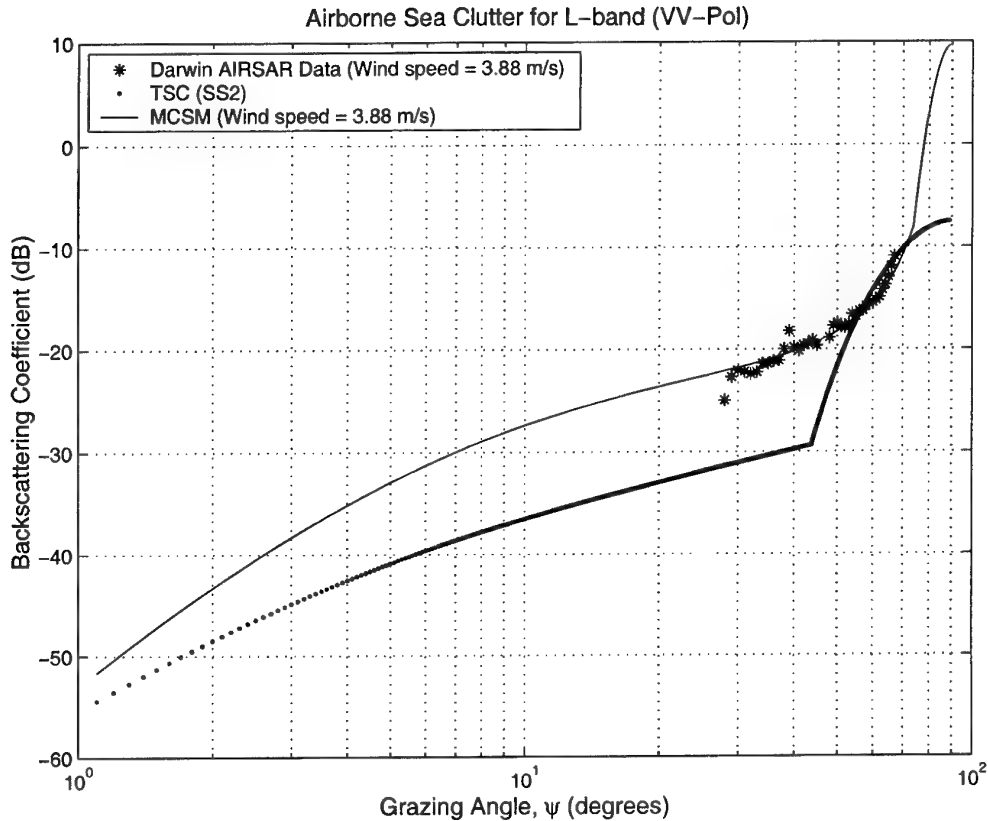


Figure 6.8: Dependence of σ° on Grazing Angle (L-VV, wind speed = 3.88 m/s)

systems under varying sea conditions, radar look directions and grazing angles. By covering a wide range of sea conditions, we were able to select the most appropriate sea clutter model. These results suggested that among these four (*GIT*, *HYB*, *TSC*, *MCSM*) sea clutter models, the *MCSM* model is the better generic sea clutter model for predicting the sea surface backscattering coefficient, σ° , for an L-band, VV-polarised radar system.

We have not considered the inclusion of contributions from wedge scattering proposed by Lyzenga and associates [24], due to several reasons. Firstly, it is impossible to measure the number of wedges per square meter, and their average length. Secondly, it has been noted by Lyzenga that for vertical polarisation, there is good agreement between Bragg scattering and the NRL-4FR data with minimal contribution from wedge scatterers. Thirdly, at L-band, the wedge appear to reach saturation and break slower compare to X-band wedges. In view of this, the contributions from Bragg scatterers can be extended to low grazing angles for L-band VV-polarised system.

7 Radar Backscattering Signals from Darwin Coastal Areas

For a radar system operating close to the coastal region, its detection and tracking capabilities will be severely affected by compounded backscatter reflections from the coastal water, foreshore vegetation, and man-made structures. The clutter return from the coastal land areas will depend on the coastal terrain characteristics e.g., vegetation type, presence of man-made structure, ground surface roughness and many more.

Calibrated POLSAR images of the Darwin areas, CM5512 and CM5148 shown in Figures 3.4 and 3.5 were used to study the properties of mean backscattering coefficient, σ^0 , from coastal water and terrain. The availability of the Darwin POLSAR data allows us to study the characteristics of backscatter signals from coastal water, coastal saline flat and mangrove forest and their dependence on grazing angle for an L-band VV-polarised radar system. Terrain scatterer types in the POLSAR images were identified using the TOPO-100K and TOPO-50K maps.

7.1 Coastal Water Backscattering Characteristics

The radar signal backscatter from the coastal water surface close to the coastal saline flat of the Darwin coast at low-tide were measured from the POLSAR images. As shown

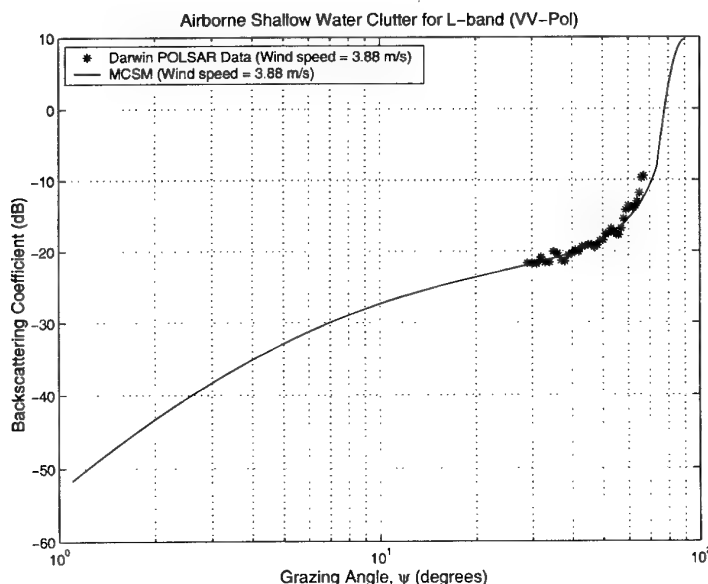


Figure 7.1: Radar Backscattering Coefficients from Shallow Water Surface

in Figure 7.1, the *MCSM* sea clutter model has good agreement with the measured coastal water backscattered values. However, with increasing grazing angles the returns increases more rapidly than that predicted by the *MCSM* sea clutter model.

7.2 Wetland Features

Radar backscatter from wetland is dependent on the tide conditions. At high tide, the sea water will completely cover the aerial roots, resulting in a reduction in multipath backscatter aerial-ground interaction (D) shown in Figure 7.2. At the same time, flooded mangrove forest have a smoother surface than a non-flooded surface. Radar backscatter from a flooded surface tends to be higher by 3 - 10 dB compared to non-flooded surface [28]. L-band signals are able to penetrate the vegetation canopy to cause either direct or multipath reflection on the smooth water surface (A,C,D).

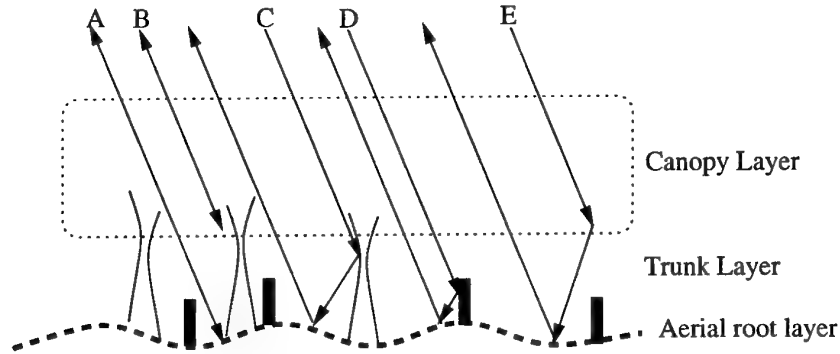


Figure 7.2: Backscatter components of wetlands. A = surface backscatter. B = canopy backscatter. C = double bounce trunk-surface backscatter. D = double bounce aerial-surface backscatter. E = double bounce canopy-surface backscatter. [48]

7.2.1 Radar Backscattering from Coastal Saline Flat Surfaces (A)

L-VV backscattered values from coastal saline flat surfaces under non-flooded conditions were evaluated from the POLSAR images of Figures 3.4 and 3.5 for varying grazing angles. The radar backscattering characteristic, σ° , dependence on grazing angles for coastal saline flat is shown in Figure 7.3. The result shows an increasing trend in backscatter with increasing grazing angles.

The *Small Perturbation Model* (SPM) has been used to calculate the backscattering and specular reflection from the coastal saline flat surfaces for an L-band radar. The backscattering coefficient, σ_{spp}° , is given by [43, 11]

$$\sigma_{spp}^\circ = 8(kh_{rms})^2 \cos^4 \theta_i \underbrace{W(2k_o \sin \theta_i, 0)}_{\text{Roughness Spectrum}} |\alpha_{pp}|^2 \quad (25)$$

where

- k_o = radar wavenumber ($k_o = \frac{2\pi}{\lambda}$);
- h_{rms} = surface rms roughness (m);
- L = surface correlation length (m);
- θ_i = incidence angle (radian);
- α_{pp} = scattering coefficient.

Note that the SPM method is valid only if $kh_{rms} < 0.3$ and $kL < 3$ [31].

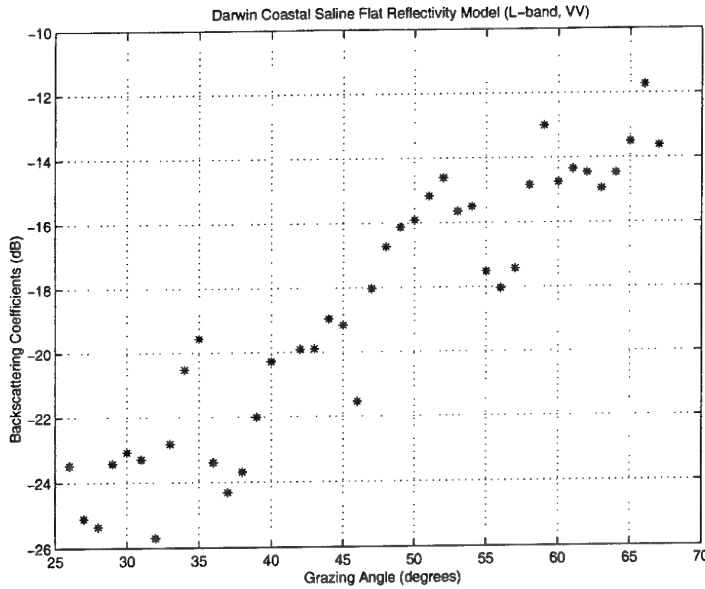


Figure 7.3: Radar Backscattering from Coastal Saline Flat

1. The first order scattering coefficient, α_{pp} [16]

$$\begin{aligned} \text{Horizontal Polarisation, } \alpha_{HH} &= \frac{(\epsilon_r - 1)}{[\cos \theta_i + \sqrt{(\epsilon_r - \sin^2 \theta_i)}]^2} \\ \text{Vertical Polarisation, } \alpha_{VV} &= \frac{(\epsilon_r - 1)[\epsilon_r(1 + \sin^2 \theta_i) - \sin^2 \theta_i]}{[\epsilon_r \cos \theta_i + \sqrt{(\epsilon_r - \sin^2 \theta_i)}]^2} \end{aligned} \quad (26)$$

where ϵ_r is the relative dielectric constant of the coastal saline flat surface.

2. Surface Roughness Spectrum

Gaussian Correlation Coefficient [31, 43]

For a 1st order Gaussian correlation coefficient of the form, $\rho(\xi) = \exp(-\xi^2/L^2)$, the isotropic surface roughness spectrum is given by the zero-order *Hankel* transform,

$$\begin{aligned} W(2k_o \sin \theta_i, 0) &= H_0\{\rho(\xi)\} \\ &= \frac{L^2}{2} \exp[-(kL \sin \theta_i)^2] \end{aligned} \quad (27)$$

$h_{rms} = 0.033$ cm and $L = 9.2$ cm, and a dielectric constant of $72 - j59$ for the coastal saline flat surface were assumed in the simulation. The basis for these assumptions lies in the reality of the coastal saline flat surface conditions: (1) the area is very level; and (2) because of the twice daily inundation of sea water at high-tide, the non-flooded coastal saline flat surface is saturated with sea water. Therefore the dielectric property of the coastal saline flat surface is similar to that of the sea water [48]. However, the dielectric content will vary during the monsoon rainy season due to the dilution of the salt water. Figure 7.4 shows the measured coastal saline flat data, and the predicted σ_{VV}^o values by the *SPM* clutter model with Gaussian correlation coefficient.

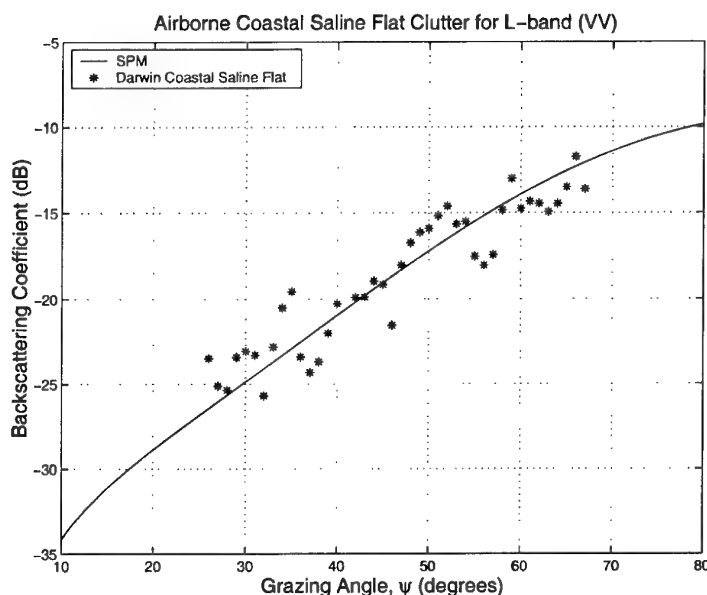


Figure 7.4: L-VV Backscattering Prediction for Non-flooded Coastal Saline Flat Surfaces

Comparison of the predicted backscattering with the POLSAR data shows good agreement for returns from non-flooded coastal saline flat surfaces. However, due to the limited data available, further validation would have to be carried out to assess the suitability of the *SPM* model in predicting backscatter from non-flooded coastal saline flat surface.

7.2.2 Radar Backscattering from Coastal Mangrove Forest

The double-bounce ground ↔ trees/ aerial roots backscatter signal is enhanced by the presence of sea water under the *Rhizophora stylosa* trees. The strong double-bounce backscattered signal is observed along the unshadowed foreshore section of the coastal Darwin areas. Mouchot and Garello [27] also noted that the presence of vertical structure of vegetation in both swamps and mangrove forest relative to the surface of the sea acts as a corner reflector, resulting in an area of bright return for L-band radars.

Strong returns can be seen from mangrove forest surrounding the coastal Darwin areas in Figures 3.4 and 3.5. Richard and associates [36] have shown that the specular returns from tree trunks to ground and then back to the radar system give rise to higher scattering levels in comparison to volume scattering from the canopy or returns from the ground surface. Measured backscatter signal from the mangrove forest surrounding the coastal Darwin areas is shown in Figure 7.5 to increase with grazing angles. This could be partly explained by the shorter path length through the canopy and trunk layers at higher grazing angles.

Models relating the structure and geometry of the mangrove forest were not carried out due to the lack ground truth information.

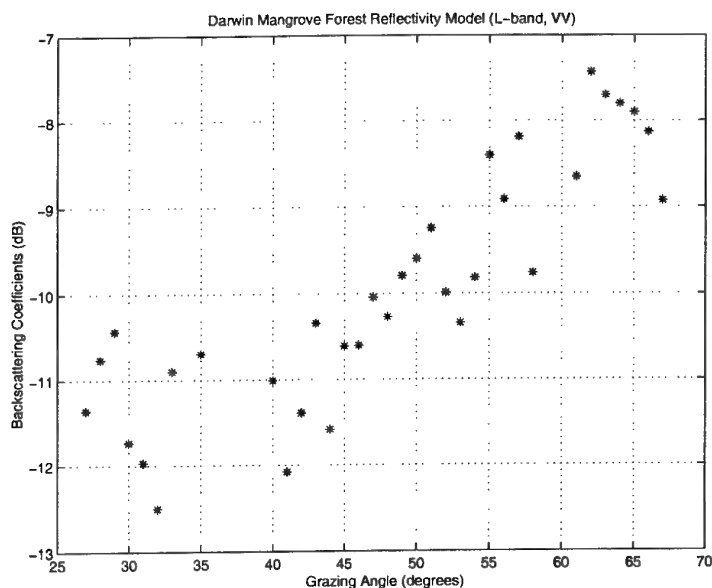


Figure 7.5: Radar Backscattering from Mangrove Forest (L-VV)

8 Conclusions

Data obtained from the NRL 4FR system (NRL-4FR, JOSS I, JOSS II), Nathanson compiled measurements, and the POLSAR Darwin datasets have been collated with five sea clutter models (*GIT*, *HYB*, *TSC*, *CSM*, and *MCSM*). These datasets were used to determine the validity of the five sea clutter models in predicting the backscatter signals from the sea surface for varying sea conditions, radar look directions and grazing angles.

The result of the comparisons have shown that the two-scale model modified for anisotropic sea spectrum, *MCSM*, accurately predicted the NRL-4FR, JOSS I, and JOSS II data for a wide range of grazing angles, look angles, and sea conditions. In addition, the *MCSM* sea clutter model accurately predicted the measured backscattering coefficients, σ° , for sea surface around the Port Darwin area for grazing angles between 25° to 65° . However, this model will have to be verified with backscattered signal acquired near normal incidence from sea temperature around 30°C .

Note that the work in this report has been primarily aimed at L-band VV-polarised radar system. Further research will have to be carried out to assess the suitability of applying the *MCSM* model to predict the sea backscattering coefficient, σ° , for varying sea conditions for radar systems operating in other frequency bands.

Acknowledgements

The author would like to acknowledge the contributions of Drs. Nick Stacy, and Ed Kruzins (and team) for providing the POLSAR Darwin images and ground truth data.

Appendix A: POLSAR Mean Backscattering Coefficients, σ° (Darwin Data)

The data in this section are organised by sea and terrain categories in Table A1 to A4. For each category, the table provides a statistical summary of the measured L-band VV-polarised backscattered POLSAR Darwin data. At each grazing angle for which data are measured, the following information is provided in the statistical distribution tables.

1. ψ , the grazing angle in degrees
2. N , the number of independent samples of pixels used in the measurement process that led to each σ° .
3. σ° , the normalised mean backscattering coefficients in dB.
4. The median, standard deviation, minimum, and maximum values of the σ° distribution, expressed in dB.

Table A1: Backscattering Coefficient for Deep Water for L-VV POLSAR Darwin

ψ	N Samples	σ^0 (dB)	Median (dB)	Std. Dev. (dB)	Min (dB)	Max (dB)
28	828	-24.96	-25.50	2.55	-34.50	-19.00
29	54648	-22.69	-23.00	2.06	-35.25	-12.50
30	56942	-22.07	-22.50	2.24	-37.50	-15.00
31	76018	-22.18	-22.50	2.34	-39.25	-15.50
32	77080	-22.40	-22.75	2.33	-40.00	-15.75
33	63390	-22.23	-22.50	2.84	-40.00	-15.25
34	41400	-21.40	-21.75	2.06	-39.50	-15.00
35	38916	-21.39	-21.75	1.99	-33.00	-6.75
36	45284	-21.17	-21.50	2.13	-34.50	-5.75
37	43900	-21.09	-21.50	2.20	-34.00	-5.50
38	33948	-20.01	-21.25	2.70	-36.00	7.25
39	32292	-18.21	-21.00	2.96	-33.25	11.75
40	31050	-19.83	-20.50	2.41	-35.00	3.25
41	23184	-20.15	-20.50	2.26	-33.50	-11.75
42	7644	-19.63	-20.00	2.30	-35.25	-13.75
43	11368	-19.47	-19.75	2.37	-36.25	-12.00
44	10976	-19.12	-19.50	2.47	-36.50	-2.25
45	10388	-19.66	-20.00	3.00	-36.50	-12.75
48	3838	-18.89	-19.25	1.91	-27.50	-13.75
49	4747	-17.73	-18.00	1.87	-25.50	-10.00
50	4646	-17.44	-17.75	1.89	-26.50	-11.50
51	8532	-17.84	-18.25	1.90	-27.75	-12.25
52	10722	-17.92	-18.25	2.52	-35.25	-7.50
53	22972	-17.54	-18.25	3.85	-40.00	-8.75
54	24477	-16.57	-17.00	3.70	-40.00	0.00
55	35139	-16.77	-17.25	3.09	-40.00	0.00
56	39671	-16.28	-16.75	2.88	-40.00	0.00
57	32984	-16.21	-16.75	2.67	-40.00	0.00
58	36026	-15.82	-16.25	2.46	-36.75	-8.75
59	46881	-15.51	-16.00	2.63	-35.25	-7.00
60	48099	-15.44	-15.75	2.93	-36.75	-4.25
61	47190	-15.16	-15.50	2.90	-36.00	-3.50
62	47020	-14.90	-15.25	2.76	-35.50	-2.00
63	45906	-14.16	-14.50	2.47	-34.50	-3.50
64	44698	-13.67	-14.00	2.46	-30.50	-6.75
65	43584	-12.92	-13.25	2.58	-28.00	-6.00
66	44206	-11.85	-12.25	2.20	-40.00	-5.50
67	21211	-10.90	-11.25	2.36	-40.00	-4.25

Table A2: Backscattering Coefficient for Coastal Water for L-VV POLSAR Darwin

ψ	N Samples	σ^0 (dB)	Median (dB)	Std. Dev. (dB)	Min (dB)	Max (dB)
29	4087	-21.69	-22.00	1.87	-29.25	-16.75
30	8701	-21.70	-22.00	2.64	-40.00	-15.75
31	17413	-21.79	-22.25	2.82	-39.25	-14.50
32	6250	-20.89	-21.25	2.52	-37.25	-14.00
33	3625	-21.61	-22.00	2.84	-38.00	-15.25
34	2418	-21.57	-22.25	2.48	-33.75	-15.25
35	10130	-20.08	-20.75	2.82	-35.25	-13.75
36	22201	-20.34	-20.75	2.38	-34.00	-12.00
37	11708	-21.32	-21.75	2.45	-39.25	-14.50
38	6042	-21.47	-21.75	2.32	-35.25	-15.25
39	11346	-20.57	-21.00	2.22	-33.50	-14.00
40	7093	-20.31	-20.75	2.43	-32.75	-14.25
41	4533	-19.87	-20.25	2.14	-32.50	-13.50
42	6473	-20.11	-20.50	2.13	-32.00	-15.00
43	3087	-19.38	-19.75	2.03	-29.75	-13.00
44	8079	-19.33	-19.75	2.04	-29.00	-13.00
45	7534	-19.11	-19.50	1.88	-28.75	-14.00
46	5784	-19.14	-19.50	1.98	-29.75	-12.75
47	4544	-19.48	-19.75	1.94	-29.75	-14.75
48	1533	-19.23	-19.50	1.92	-26.50	-12.00
49	3068	-18.53	-18.75	1.88	-25.75	-14.25
50	4692	-18.46	-18.75	1.96	-28.75	-12.25
51	3960	-17.60	-18.00	1.90	-25.75	-11.50
52	3990	-17.50	-17.75	2.10	-26.50	-10.25
53	3876	-16.87	-17.25	1.98	-26.50	-11.25
54	3923	-17.32	-17.75	2.06	-25.00	-11.75
55	4606	-17.68	-18.00	1.92	-25.50	-10.75
56	1549	-17.76	-18.00	1.84	-24.75	-13.75
57	3555	-16.82	-17.00	1.80	-26.00	-11.00
58	3397	-15.45	-15.75	1.84	-24.75	-10.75
59	2636	-14.22	-14.50	1.96	-22.00	-8.50
60	6399	-13.63	-14.00	2.01	-23.50	-7.00
61	5661	-13.88	-14.25	1.89	-23.75	-8.00
62	3567	-13.97	-14.25	1.82	-21.00	-8.75
63	5418	-13.70	-14.00	1.85	-22.25	-7.75
64	7536	-13.03	-13.25	1.85	-25.50	-8.00
65	5437	-11.83	-12.50	2.20	-20.00	-5.50
66	930	-9.72	-10.00	1.81	-17.50	-5.50
67	840	-9.43	-9.75	1.80	-16.75	-5.00

Table A3: Backscattering Coefficient for Coastal Saline Flat for L-VV POLSAR Darwin

ψ	N Samples	σ° (dB)	Median (dB)	Std. Dev. (dB)	Min (dB)	Max (dB)
26	11178	-23.49	-26.75	4.81	-40.00	-8.50
27	19238	-25.11	-26.00	2.77	-36.75	-14.75
28	1859	-25.35	-29.00	5.90	-40.00	-15.50
29	28523	-23.42	-24.75	4.24	-40.00	-9.75
30	15322	-23.07	-24.75	4.11	-38.75	-7.50
31	21869	-23.30	-24.50	3.37	-36.25	-13.25
32	40784	-25.70	-27.75	3.53	-38.00	-12.50
33	3646	-22.82	-24.00	3.77	-36.50	-14.00
34	5404	-20.52	-21.25	2.54	-31.25	-13.50
35	4808	-19.56	-21.00	2.85	-31.25	-11.00
36	9121	-23.40	-24.25	3.53	-37.50	-12.25
37	10898	-24.32	-25.25	3.35	-36.25	-17.75
38	10217	-23.69	-24.25	3.39	-37.50	-16.00
39	506	-22.01	-22.75	2.52	-30.25	-14.50
40	744	-20.29	-21.25	2.77	-29.25	-13.50
42	1722	-19.91	-20.75	2.57	-29.50	-11.25
43	2860	-19.89	-20.50	2.47	-31.25	-13.25
44	1707	-18.96	-19.75	2.55	-28.25	-10.50
45	486	-19.16	-20.00	2.59	-29.50	-13.00
46	3851	-21.55	-22.50	2.69	-32.25	-12.75
47	9378	-18.03	-19.00	3.58	-32.75	-9.75
48	10830	-16.73	-18.25	3.87	-37.75	-6.75
49	15697	-16.13	-18.75	4.72	-36.50	-4.50
50	15580	-15.91	-18.00	4.57	-37.75	-3.50
51	18824	-15.17	-17.00	4.10	-34.50	-4.50
52	13614	-14.61	-16.25	4.18	-36.00	-3.75
53	17721	-15.65	-17.50	4.21	-37.25	-3.50
54	16459	-15.50	-17.00	4.62	-39.50	-5.00
55	13096	-17.52	-19.00	3.25	-31.00	-5.75
56	12040	-18.04	-20.25	3.57	-29.75	-5.00
57	10179	-17.43	-19.25	3.31	-29.75	-4.75
58	4827	-14.84	-15.50	2.99	-30.25	-7.00
59	196	-13.00	-13.37	2.10	-21.00	-8.25
60	3435	-14.75	-15.25	2.18	-23.00	-7.50
61	1281	-14.34	-14.75	1.95	-22.50	-9.00
62	8513	-14.46	-16.50	6.28	-36.75	-2.00
63	11399	-14.94	-17.25	5.78	-37.50	-2.75
64	10983	-14.47	-17.50	5.40	-34.75	0.00
65	13363	-13.51	-15.50	5.11	-34.75	-2.25
66	17312	-11.74	-12.75	4.04	-33.00	1.75
67	3701	-13.62	-14.75	2.99	-27.25	-5.00

Table A4: Backscattering Coefficient for Mangrove Forest for L-VV POLSAR Darwin

ψ	N Samples	σ° (dB)	Median (dB)	Std. Dev. (dB)	Min (dB)	Max (dB)
27	194	-11.36	-12.12	2.87	-19.50	-6.00
28	99	-10.76	-11.00	2.44	-18.50	-6.00
29	28	-10.43	-10.99	2.55	-15.75	-5.50
30	142	-11.73	-12.75	2.97	-20.00	-6.75
31	164	-11.97	-12.62	2.39	-18.75	-8.00
32	52	-12.50	-12.75	2.64	-21.50	-8.75
33	42	-10.90	-11.50	2.86	-19.75	-5.25
35	46	-10.69	-11.50	2.80	-18.00	-5.50
40	75	-11.01	-11.75	2.30	-17.75	-5.00
41	29	-12.08	-13.00	1.72	-15.25	-8.50
42	99	-11.39	-11.75	1.98	-17.75	-8.00
43	105	-10.34	-11.25	2.48	-19.00	-4.75
44	82	-11.59	-12.00	2.58	-18.25	-6.25
45	114	-10.61	-11.12	2.57	-19.75	-4.25
46	103	-10.60	-11.00	2.31	-18.25	-6.50
47	178	-10.04	-11.00	2.67	-18.75	-4.00
48	87	-10.27	-10.75	2.20	-16.50	-6.50
49	47	-9.80	-10.50	2.03	-14.50	-6.25
50	46	-9.60	-10.12	2.15	-14.25	-6.25
51	44	-9.24	-10.25	2.57	-15.75	-4.50
52	76	-9.99	-10.62	1.93	-15.00	-6.50
53	55	-10.34	-10.75	2.15	-16.75	-6.75
54	85	-9.82	-10.25	2.39	-18.75	-3.25
55	87	-8.40	-9.00	2.34	-15.25	-3.25
56	77	-8.91	-9.75	2.79	-16.50	-2.75
57	41	-8.19	-9.25	2.78	-14.50	-1.00
58	8	-9.76	-10.75	2.41	-14.50	-7.00
61	28	-8.65	-9.86	3.17	-17.00	-4.50
62	52	-7.43	-8.37	2.64	-17.00	-2.00
63	51	-7.70	-8.25	2.49	-14.00	-3.25
64	9	-7.80	-7.25	2.68	-13.50	-5.25
65	41	-7.90	-9.25	3.11	-14.00	-3.00
66	72	-8.13	-8.62	2.30	-13.25	-3.00
67	50	-8.93	-9.25	1.88	-14.00	-5.25

Appendix B: Semi-Empirical Sea Clutter Models

B.1 Georgia Institute of Technology (GIT) Sea Clutter Model

[32, 1]

(a) Reflectivity equations, (dB m²/m²)

For horizontal polarisation,

$$\sigma_{HH}^{\circ} = 10 \log[3.9 \times 10^{-6} \lambda \psi^{0.4} G_m G_u G_w] \quad (B1)$$

For vertical polarisation,

$$\sigma_{VV}^{\circ} = \sigma_{HH}^{\circ} - 1.73 \ln(h_a + 0.015) + 3.76 \ln(\lambda) + 2.46 \ln(\psi + 0.0001) + 22.2 \quad (B2)$$

(b) Interference Factor

$$\begin{aligned} G_m &= \frac{a^4}{(1 + a^4)} \\ a &= \frac{(14.4\lambda + 5.5)\psi h_a}{\lambda} \\ \text{Average wave height, } h_a(m) &= 4.52 \times 10^{-3} V_w^{2.5} \end{aligned}$$

(c) Wind Direction Factor

$$G_u = \exp\{0.2 \cos \phi (1 - 2.8\psi)(\lambda + 0.015)^{-0.4}\}$$

(d) Wind Speed Factor

$$\begin{aligned} G_w &= \left[\frac{1.94 V_w}{(1 + V_w/15.4)} \right]^q \\ q &= \frac{1.1}{(\lambda + 0.015)^{0.4}} \end{aligned}$$

where

- ψ = grazing angle (radians);
- λ = radar wavelength (m);
- V_w = wind speed (m/s)

B.2 Hybrid (HYB) Sea Clutter Model [35, 1]

- (a) Reflectivity equations, (dB m²/m²),

$$\sigma^\circ = \sigma^\circ(\text{ref}) + K_g + K_s + K_p + K_d \quad (\text{B3})$$

- (b) Reference Reflectivity (dB m²/m²) for $\psi = 0.1^\circ$, $\phi = 0^\circ$, VV polarisation and sea state 5.

$$\sigma^\circ(\text{ref}) = 24.4 \log f - 65.2 \quad (\text{B4})$$

- (c) Grazing Angle adjustments, K_g (dB)

Reference Grazing Angle ($^\circ$), $\psi_r = 0.1^\circ$

Transitional Angle ($^\circ$), $\psi_t = \sin^{-1}(0.0632\lambda/h_{RMS})^\circ$

RMS Wave Height (m), $h_{RMS} = 0.031.SS^2$ where SS = Douglas Sea State

- (i) For $\psi_t \geq \psi_r$,

$$K_g = \begin{cases} 0, & \text{for } \psi < \psi_r, \\ 20 \log \frac{\psi}{\psi_r}, & \text{for } \psi_r \leq \psi \leq \psi_t, \\ 20 \log \frac{\psi_t}{\psi_r} + 10 \log \frac{\psi}{\psi_t}, & \text{for } \psi_t < \psi < 30^\circ. \end{cases}$$

- (ii) For $\psi_t < \psi_r$,

$$K_g = \begin{cases} 0, & \text{for } \psi \leq \psi_r, \\ 10 \log \frac{\psi}{\psi_r}, & \text{for } \psi > \psi_r. \end{cases}$$

- (d) Sea State Adjustment (dB), $K_s = 5(SS - 5)$

- (e) Polarisation Adjustment, K_p (dB),

- (i) Average Wave Height (m), $h_a = 0.08SS^2$

- (ii) Vertical Polarisation, $K_p = 0$

- (iii) Horizontal Polarisation,

$$K_p = 1.7 \ln(h_a + 0.015) - 3.8 \ln \lambda - 2.5 \ln \left(\frac{\psi}{57.3} + 0.0001 \right) - 22.2, \quad (\text{B5})$$

- (f) Wind Direction Adjustment, K_d (dB)

$$K_d = \left(2 + 1.7 \log \frac{0.1}{\lambda} \right) (\cos \phi - 1) \quad (\text{B6})$$

where ϕ is the radar look angle with respect to the wind direction ($\phi = 0$ for upwind).

B.3 Technology Service Corporation (TSC) Sea Clutter Model [40]

(a) Low Angle Factor, G_A

$$\text{Surface height standard deviation, } \sigma_z = 0.115.SS^{1.95} \quad (B7)$$

$$\sigma_\alpha = 14.9.\psi \frac{\sigma_z + 0.25}{\lambda} \quad (B8)$$

$$G_A = \sigma_\alpha^{1.5} / (1 + \sigma_\alpha^{1.5}) \quad (B9)$$

where

ψ = grazing angle (radians);

λ = radar wavelength (ft.);

SS = Sea state (Douglas sea state);

σ_z = sea surface height standard deviation.

(b) Wind Speed Factor, G_w

$$\text{Wind velocity, } V_w = 6.2.SS^{0.8} \quad (B10)$$

$$Q = \psi^{0.6}$$

$$A_1 = \left[1 + \left(\frac{\lambda}{0.03} \right)^3 \right]^{0.1}$$

$$A_2 = \left[1 + \left(\frac{\lambda}{0.1} \right)^3 \right]^{0.1}$$

$$A_3 = \left[1 + \left(\frac{\lambda}{0.3} \right)^3 \right]^{Q/3}$$

$$A_4 = 1 + 0.35.Q$$

$$A = \frac{2.63A_1}{A_2A_3A_4}$$

$$G_w = \left[\frac{V_w + 4.0}{15} \right]^A$$

(c) Aspect Factor, G_u

$$G_u = \begin{cases} 1, & \phi = \frac{\pi}{2} \\ \exp \left(0.3 \cos \phi \cdot \frac{\exp(-\psi/0.17)}{(\lambda^2 + 0.005)^{0.2}} \right), & \text{otherwise} \end{cases} \quad (B11)$$

where ϕ (radians) is the wind direction angle relative to the line-of-sight.

(d) Reflectivity ($\frac{m^2}{m^2}$)

For horizontal polarisation (dB),

$$\sigma_{HH}^\circ = 10 \log_{10} \left[1.7 \times 10^{-5} \psi^{0.5} \frac{G_u G_w G_A}{(\lambda + 0.05)^{1.8}} \right] \quad (B12)$$

For vertical polarisation (dB),

$$\sigma_{VV}^{\circ} = \sigma_{HH}^{\circ} - 10 \log_{10} [1.73 \ln(2.507\sigma_z + 0.05) + 3.76 \ln \lambda + 2.46 \ln(\sin \psi + 0.0001) + 19.8] \quad (\text{B13})$$

(d) Specular Returns

For horizontal and vertical polarisation,

$$\sigma_{VV}^{\circ} = \sigma_{HH}^{\circ} = \mu \cot^2 \beta_{\circ} \exp \left(-\frac{\tan^2 \theta}{\tan^2 \theta_{\circ}} \right) \quad (\text{B14})$$

where

$$\begin{aligned} \theta &= \pi/2 - \psi \\ 10 \log \mu &= -5 + 12.5(\log \lambda - \log(0.5)) \text{ dB} \\ \beta_{\circ} &= \begin{cases} 10.1 + 1.65 SS, & SS \leq 2 \\ 13.4 + 0.7(SS - 2), & SS > 2 \end{cases} \end{aligned} \quad (\text{B15})$$

References

1. Antipov, I. (1998) *Simulation of Sea Clutter Returns*, Technical Report DSTO-TR-0679, Defence Science and Technology Organisation, Salisbury.
2. Barrick, D. (1974) Wind Dependence of Quasi-Specular Microwave Sea Scatter, *IEEE Trans. Antenna and Propagation* **AP-22**, 135-136.
3. Brocklehurst, P. & Edmeades, B. (1996) *The Mangrove Communities of Darwin Harbour*, Technical Report 96/9, Department of Lands, Planning & Environment.
4. Chan, H. (1990) Radar sea-clutter at low grazing angles, *IEE Proceedings* **137**(2), 102-112.
5. Chen, K., Fung, A. & Weissman, D. (1992) A Backscattering Model for Ocean Surface, *IEEE Trans. Geoscience and Remote Sensing* **30**(4), 811-817.
6. Cox, C. & Munk, W. (1954) Measurement of the Roughness of the Sea Surface from Photographs of the Sun's Glitter, *J. Optical Society of America* **44**(11), 838-850.
7. Daley, J. (1973) Wind Dependence of Radar Sea Return, *J. Geophys. Res.* **78**(33), 7823-7833.
8. Daley, J., Davis, W. & Mills, N. (1970) *Radar Sea Return in High Sea States*, Technical Report NRL Report 7142, Naval Research Laboratory, Wave Propagation Branch, Electronics Division.
9. Daley, J., J.T. Ransone, J. & Burkett, J. (1971) *Radar Sea Return - JOSS I*, Technical Report NRL Report 7268, Naval Research Laboratory, Wave Propagation Branch, Electronics Division.
10. Daley, J., J.T. Ransone, J. & Davis, W. (1973) *Radar Sea Return - JOSS II*, Technical Report NRL Report 7534, Naval Research Laboratory, Radar Division.
11. Dobson, M. & Ulaby, F. (1986) Preliminary Evaluation of SIR-B Response to Soil Moisture, Surface Roughness, and Crop Canopy Cover, *IEEE Trans. Geoscience and Remote Sensing* **GE-24**(4), 517-526.
12. Dockery, G. (1990) Method for modelling sea surface clutter in complicated propagation environments, *IEE Proc.* **137**(F-2), 73-79.
13. Donelan, M. & W.J. Pierson, J. (1987) Radar Scattering and Equilibrium Ranges in Wind-Generated Waves With Application to Scatterometry, *J. Geophys. Res.* **92**(C5), 4971-5029.
14. Fung, A. & Lee, K. (1982) A Semi-Empirical Sea Spectrum Model for Scattering Coefficient Estimation, *IEEE J. Oceanic Eng.* **OE-7**(4), 166-176.
15. Fung, A., Chen, K. & Chen, M. (1989) A Note on the Directional Spectrum, *Remote Sens. Environ.* **30**, 95-106.
16. Guinard, N. & Daley, J. (1970) An Experimental Study of a Sea Clutter Model, *Proc. IEEE* **58**(4), 543-550.

17. Guissard, A., Baufays, C. & Sobieski, P. (1986) Sea Surface Description Requirements for Electromagnetic Scattering Calculations, *J. Geophys. Res.* **91**(C2), 2477-2492.
18. Jao, J. (1984) Amplitude Distribution of Composite Terrain Radar Clutter and the K-distribution, *IEEE Trans. Antenna and Propagat.* **32**(10), 1049-1062.
19. Katzin, M. (1957) On the Mechanism of Radar Sea Clutter, *Proceedings of the IRE* **45**(1), 44-54.
20. Lee, P., Barter, J., Beach, K., Lake, B., Rungaldier, H., Thompson, H., Wang, L. & Yee, R. (1999) What are the mechanism for non-Bragg scattering from water wave surfaces?, *Radio Science* **34**(1), 123-138.
21. Long, M., ed. (1991) *Airborne Early Warning Concepts*, Artech House Inc., chapter 2. *AEW Radar Concepts*, pp. 205-292.
22. Long, M. W. (1983) *Radar Reflectivity of Land and Sea*, Artech House, Inc.
23. Lyzenga, D. & Bennett, J. (1988) Full-Spectrum Modeling of Synthetic Aperture Radar Internal Wave Signatures, *J. Geophys. Res.* **93**(C10), 12345-12354.
24. Lyzenga, D., Maffett, A. & Shuchman, R. (1983) The Contribution of Wedge Scattering to the Radar Cross Section of the Ocean Surface, *IEEE Trans. Geoscience and Remote Sensing* **GE-21**(4), 502-505.
25. Morchin, W. C. (1990) *Airborne Early Warning Radar*, Artech House, INC., Norwood, MA 02062.
26. Morris, G. (1988) *Airborne Pulsed Doppler Radar*, Artech House.
27. Mouchot, M. & Garello, R. (1998) *Principles & Applications of Imaging Radar Manual of Remote Sensing*, Vol. 2, 3 edn, John Wiley & Sons Inc., chapter 12. *SAR for Oceanography*, pp. 631-675.
28. Mougin, E., Proisy, C., Marty, G., Fromard, F., Puig, H., Betoulle, J. & Rudant, J. (1999) Multifrequency and Multipolarization Radar Backscattering from Mangrove Forests, *IEEE Trans. Geoscience and Remote Sensing* **37**(1), 94-102.
29. Nathanson, F. E., Reilly, J. & Cohen, M. (1999) *Radar Design Principles*, second edn, Scitech Pub., Inc., NJ, USA.
30. Neelakanta, P., DeGross, D. & Sudhakar, R. (1992) Low-Altitude Target Detection by Coastline Operated Marine Radar, *IEEE Trans. Aerospace and Electronic Systems* **28**(1), 217-222.
31. Oh, Y., Sarabandi, K. & Ulaby, F. (1992) An Empirical Model and Inversion Technique for Radar Scattering from Bare Soil Surfaces, *IEEE Trans. Geoscience and Remote Sensing* **30**(2), 370-381.
32. Paulus, R. (1990) Evaporation Duct Effects on Sea Clutter, *IEEE Transactions on Antennas and Propagation*.

33. Phillips, O. (1988) Radar Returns from the Sea Surface - Bragg Scattering and Breaking Waves, *J. Phys. Oceanography* **18**, 1065-1074.
34. Plant, W., Weissman, D., Keller, W., Hessany, V., Hayes, K. & Hoppel, K. (1999) Air/sea momentum transfer and the microwave cross section of the sea, *J. Geophys. Res.* **104**(C5), 11173-11191.
35. Reilly, J. & Dockery, G. (1990) Influence of evaporation ducts on radar sea return, *IEE Proceedings-F* **137**(2), 80-88.
36. Richards, J. & Sun, G. (1987) L-band Radar Backscatter Modelling of Forest Stands, *IEEE Trans. Geoscience and Remote Sensing* **GE-25**(4), 487-498.
37. Ryan, J. & Johnson, M. (1990) *Modelling Radar Sea Clutter*, Technical Report W7714-9-9257/01-ST, For Defence Research Establishment Ottawa.
38. Schuler, D. (1978) Remote sensing of directional gravity wave spectra and surface currents using a microwave dual frequency radar, *Radio Science* **13**(2), 321-331.
39. Skolnik, M., ed. (1990) *Radar Handbook*, 2 edn, McGraw Hill, chapter Sea Clutter, pp. 13.1-13.5.
40. Technology Service Corporation (1990) Section 5.6.1. Backscatter from Sea, in *Radar Workstation*, Vol. 2, pp. 177-186.
41. Thompson, T., Weissman, D. & W.T.Liu (1986) *Marineland Aircraft Observations of L-band Radar Backscatter Dependence Upon Wind Direction*, Plenum Press, chapter 33, pp. 491-503.
42. Ulaby, F., Moore, R. & Fung, A. (1982) *Microwave Remote Sensing: Active and Passive*, Vol. II. *Radar Remote Sensing and Surface Scattering and Emission Theory*, Artech House Inc.
43. Ulaby, F., Moore, R. & Fung, A. (1986) *Microwave Remote Sensing: Active and Passive*, Vol. III. *From Theory to Applications*, Artech House Inc.
44. Valenzuela, G. (1978) Theories for the Interaction of Electromagnetic and Oceanic Waves - A Review, *Boundary-Layer Meteorology* **13**, 61-85.
45. Valenzuela, G. & Laing, M. (1970) Study of Doppler Spectra of Radar Sea Echo, *J. Geophys. Res* **75**, 551-563.
46. Valenzuela, G., Laing, M. & Daley, J. (1971) Ocean Spectra for the High-frequency Waves as Determined from Airborne Radar Measurements, *J. Marine Res.* **29**(2), 69-84.
47. Vesecky, J. & Stewart, R. (1982) The Observation of Ocean Surface Phenomena Using Imagery From the SEASAT Synthetic Aperture Radar: An Assessment, *J. Geophys. Res.* **87**(C5), 3397-3430.
48. Wang, Y. & Imhoff, M. (1993) Simulated and observed L-HH radar backscatter from tropical mangrove forests, *Int. J. Remote Sensing* **14**(15), 2819-2828.

49. Watts, S. & Wicks, D. (1990) Empirical models for detection prediction in k-distribution radar sea clutter, *in IEEE International Radar Conference*, IEEE, pp. 189-194.
50. Weissman, D., King, D. B. & Thompson, T. W. (1979) Relationship between Hurricane Surface Winds and L-Band Radar Backscatter from the Sea Surface, *J. Applied Meteorology* pp. 1023-1034.
51. Wright, J. (1968) A New Model for Sea Clutter, *IEEE Trans. Antennas and Propagation* **AP-176**(2), 217-223.

DSTO-TR-0945

DISTRIBUTION LIST

Modelling Airborne L-band Radar Sea and Coastal Land Clutter

Poh Lian Choong

Number of Copies

DEFENCE ORGANISATION

Task Sponsor

Director General Aerospace Surveillance Systems, J. Popham	}	
Director Airborne Early Warning and Control System Project	}	1
Office, GPCAPT. M. Binskin		

S&T Program

Chief Defence Scientist	}	
FAS Science Policy	}	1
AS Science Corporate Management	}	
Director General Science Policy Development		1
Counsellor, Defence Science, London		Doc Data Sht
Counsellor, Defence Science, Washington		Doc Data Sht
Scientific Adviser to MRDC, Thailand		Doc Data Sht
Scientific Adviser Policy and Command		1
Navy Scientific Adviser		Doc Data Sht
Scientific Adviser, Army		Doc Data Sht
Air Force Scientific Adviser		1
Director Trials		1

Aeronautical and Maritime Research Laboratory

Director, Aeronautical and Maritime Research Laboratory	1
Chief, Weapons Systems Division	1
Task Manager, G. Lawrie, LOD	1

Electronics and Surveillance Research Laboratory

Director, Electronics and Surveillance Research Laboratory	Doc Data Sht
Chief, Surveillance Systems Division, Dr. B.D. Ward	1
Chief, Electronic Warfare Division	1
Research Leader, Surveillance for Air Superiority, Dr. D. Kewley	1
Head, Surveillance Sensor Processing, SSD, Dr. J. Whitrow	1
Task Manager, S. Capon, SSD	1
Author: Dr. P.L. Choong, SSD	1
Dr. N. Stacy, SSD	1
Å. Jakobsson, SSD	1

Dr. D. McDonald, SSD	1
DSTO Research Library and Archives	
Library Fishermans Bend	1
Library Maribyrnong	1
Library Salisbury	2
Australian Archives	1
Library, MOD, Pyrmont	Doc Data Sht
US Defense Technical Information Center	2
UK Defence Research Information Centre	2
Canada Defence Scientific Information Service	1
NZ Defence Information Centre	1
National Library of Australia	1
Capability Systems Staff	
Director General Maritime Development	Doc Data Sht
Director General Land Development	1
Director General C3I Development	Doc Data Sht
Director General Aerospace Development	Doc Data Sht
Navy	
SO(Science), Director of Naval Warfare, Maritime Headquarters Annex, Garden Island	Doc Data Sht
Army	
ABCA Standardisation Officer, Puckapunyal	4
SO(Science), DJFHQ(L), MILPO, Enoggera, Queensland 4057	Doc Data Sht
Air Force	
Intelligence Program	
DGSTA, Defence Intelligence Organisation	1
Manager, Information Centre, Defence Intelligence Organisation	1
Corporate Support Program	
Officer in Charge, TRS, Defence Regional Library, Canberra	1
UNIVERSITIES AND COLLEGES	
Australian Defence Force Academy Library	1
Head of Aerospace and Mechanical Engineering, ADFA	1
Deakin University Library, Serials Section (M List)	1
Hargrave Library, Monash University	Doc Data Sht

Librarian, Flinders University	1
OTHER ORGANISATIONS	
NASA (Canberra)	1
Info Australia	1
State Library of South Australia	1
Parliamentary Library of South Australia	1
ABSTRACTING AND INFORMATION ORGANISATIONS	
Library, Chemical Abstracts Reference Service	1
Engineering Societies Library, US	1
Materials Information, Cambridge Scientific Abstracts, US	1
Documents Librarian, The Center for Research Libraries, US	1
INFORMATION EXCHANGE AGREEMENT PARTNERS	
Acquisitions Unit, Science Reference and Information Service, UK	1
Library – Exchange Desk, National Institute of Standards and Technology, US	1
National Aerospace Laboratory, Japan	1
National Aerospace Laboratory, Netherlands	1
SPARES	
DSTO Salisbury Research Library	5
Total number of copies:	59

DEFENCE SCIENCE AND TECHNOLOGY ORGANISATION DOCUMENT CONTROL DATA				1. CAVEAT/PRIVACY MARKING	
2. TITLE Modelling Airborne L-band Radar Sea and Coastal Land Clutter			3. SECURITY CLASSIFICATION Document (U) Title (U) Abstract (U)		
4. AUTHOR(S) Poh Lian Choong			5. CORPORATE AUTHOR Electronics and Surveillance Research Laboratory PO Box 1500 Salisbury, South Australia, Australia 5108		
6a. DSTO NUMBER DSTO-TR-0945		6b. AR NUMBER AR-011-227		6c. TYPE OF REPORT Technical Report	
				7. DOCUMENT DATE March 2000	
8. FILE NUMBER B9505/19/4		9. TASK NUMBER AIR 99/047		11. No OF PAGES 53	
		10. SPONSOR DGASS		12. No OF REFS 51	
13. DOWNGRADING / DELIMITING INSTRUCTIONS Not Applicable			14. RELEASE AUTHORITY Chief, Surveillance Systems Division		
15. SECONDARY RELEASE STATEMENT OF THIS DOCUMENT <i>Approved For Public Release</i> OVERSEAS ENQUIRIES OUTSIDE STATED LIMITATIONS SHOULD BE REFERRED THROUGH DOCUMENT EXCHANGE, PO BOX 1500, SALISBURY, SOUTH AUSTRALIA 5108					
16. DELIBERATE ANNOUNCEMENT No Limitations					
17. CITATION IN OTHER DOCUMENTS No Limitations					
18. DEFTEST DESCRIPTORS Sea clutter L band Airborne radar Ground clutter Backscattering					
19. ABSTRACT The limiting factor affecting the performance of most airborne radar systems in detecting targets on or near wind-swept surface of the sea is return echoes from sea surface, known as sea clutter. This report addresses the clutter returns from a maritime environment for airborne L-band VV-polarised radar. Modelling of radar sea return is discussed with consideration to propagation under standard atmospheric conditions. A composite sea clutter model has been developed, which is based upon the concept of a two-scale sea surface model with directional sea spectrum and simple facet specular return at near-normal incidence. Several sea clutter models have been collated with data collected by the Naval Research Laboratory four-frequency radar system under varying sea conditions, and polarimetric synthetic aperture radar images of the North-West of Australia. The results of the comparison have shown that the composite sea clutter model better predicts the backscattering coefficient, σ^0 , of sea surface returns for varying sea conditions, radar look directions, and grazing angles. In addition, a radar backscattering model for bare soil showed good agreement between modelling results and POLSAR data for returns from coastal saline flat surfaces surrounding the North-West coastal areas.					